



Investigations on gas jet beam profiles with a Mach-Zehnder interferometer

Lukas Leßmann
lukas.lessmann@wwu.de

Master's thesis
in the department of nuclear physics
of the Westfälische Wilhelms-Universität Münster
December 23, 2016

Contents

1	Introduction	1
2	MAGIX @ MESA	5
2.1	MESA - Mainz Energy-Recovering Superconducting Accelerator	5
2.2	MAGIX - MESA Gas Internal Target EXperiment	8
3	Internal targets for fixed target experiments	13
3.1	Luminosity	14
3.2	Supersonic gas-jet targets	14
4	Mach-Zehnder interferometer	17
4.1	Principle of Mach-Zehnder interferometers	17
4.2	Fourier Transformation	25
5	The experimental setup	27
5.1	Building the experimental setup	27
5.2	Optimisation of the Mach-Zehnder interferometer	32
6	Density determination program	35
6.1	F-interpolation program	36
6.2	Fourier Transformation program	43
7	Measurements on the gas target for MAGIX	51
7.1	Comparison with theoretical calculations	51
7.2	Nitrogen jets	56
8	Summary and Outlook	59

A	Appendix	63
A.1	Reconstructed areal density profiles	63

1 Introduction

The understanding of the elements of matter and their interactions with each other has constantly grown in the last century. The most common theory to describe the basic components of matter is the standard model of particle physics. It describes quarks, leptons, gauge bosons and the Higgs boson [Ber02]. Quarks (q) never occur alone, but in pairs of quark and anti-quark called mesons ($q\bar{q}$) or in triples of quarks called baryons (qqq). The two most popular baryons are the nucleons: The neutron and the proton. There are two kinds of leptons in the standard model: Charged leptons like the electron and the very light neutrinos. The gauge bosons build three groups: The photon (γ) carries the electromagnetic force, the eight gluons (g) are the force carriers of the strong interaction and the three weak bosons (Z^0, W^\pm) carry the weak interaction.

Although the standard model fits very well for many observed phenomenons, there are many open questions. Some of them concern the still unknown mass of the neutrinos or the unification of gravity with the standard model. Others concern the electromagnetic form factor of well known particles like the proton or the neutron. And yet others are asking for additional particles such as dark matter to explain observed phenomenons in the universe. For many fields of nuclear and particle physics it is crucial to improve the standard model by answering some of these questions or by introducing new particles to explain the observed phenomenons. Modern experiments are necessary to fortify the different theories and to search for the different predicted particles.

MAGIX at the future MESA facility will be one of these experiments. MESA will be a multiturn Energy-Recovery-Linac providing an electron beam with a beam energy of 105 MeV at a very large beam current of up to 10 mA [Sim14]. This beam will be used by MAGIX for measurements on the electromagnetic form factor of the proton by

elastic electron proton scattering [MAG16]. The high beam current and a new detector design will enable smaller uncertainties of the measurements and may unify the so far contradictory values [Car15]. The same experiment will be used to search for dark photons as light dark matter by detecting their decay products after producing them in electron proton collisions. MAGIX and the linear accelerator MESA will be described in chapter 2. For measurements of MAGIX, a windowless proton target with a constant areal density of 10^{19} cm^{-2} is needed to achieve a high luminosity of $10^{35} \text{ cm}^{-2} \text{ s}^{-1}$. The high luminosity is crucial to reach a significant number of rare events like the production and decay of dark photons. The required areal density can be achieved by a supersonic gas-jet target by pressing cooled hydrogen through a Laval nozzle. Since gas-jets are stable, homogeneous and in their density adjustable targets, they are the best possible choice for MAGIX. The working principle of supersonic gas-jet targets will be presented in chapter 3. The gas-jet target for MAGIX, the MCT-M, has already been built and its components have been tested [Har16]. A new testing setup will be built in the scope of this work. It will be presented in chapter 5. The testing setup consists of the MCT-M and a Mach-Zehnder interferometer. The interferometer splits a laser beam into two equal beams and guides one of them through the gas-jet of the MCT-M. The other beam is guided around the gas-jet and the two beams are superposed after an equal path length. The different index of refraction of the gas-jet slows down the laser beam passing it and causes a phase difference between the two beams dependent on the index of refraction of the gas-jet, which is proportional to its areal density. The phase difference is visualised by the interference with the second beam. A detailed description of the working principle of Mach-Zehnder interferometers and the connection between the interference pattern and the gas-jet areal density profile will be presented in chapter 4. This method will be used to monitor the areal density profile of the gas-jet without taking any influence on it. This monitoring of the target results in a precise knowledge of the value and stability of the target density, which is very important for the data analysis of MAGIX. The evaluation of the interference pattern is not trivial. Two programs have been written to reconstruct the two dimensional (areal) density profile of the gas-jet from the interference pattern. Both programs use different methods and will be presented in chapter 6. Measurements on the areal density profile of the gas-jet of the MCT-M will be done in this work to control the maximal areal density, for investigations on the beam shape and the beam stability. Knowing the beam shape of the gas-jet can be used to design a catcher opposite to the nozzle to reduce the background for measure-

ments at MAGIX. The function of the catcher is to lead off the main part of the gas-jet behind the interaction point to improve the vacuum in the interaction chamber. This requires a stable target at the range between nozzle and catcher. The measurements are presented together with theoretical calculations on the maximal areal density in chapter 7.

2 MAGIX @ MESA

The **M**ainz **E**nergy-Recovering **S**uperconducting **A**ccelerator (MESA) is under construction right now, funded by the cluster of excellence ”**P**recision Physics, Fundamental Interactions and **S**tructure of **M**atter” (PRISMA) [MAG16]. The electron accelerator MESA will be a multiturn Energy-Recovery-Linac (ERL) aiming for measurements on dark photons, the proton charge radius and the electroweak mixing angle [MES16]. In addition it will be a test facility for bigger multiturn Energy-Recovery-Linacs like the LHeC. The design and the characteristics of MESA are described together with the planned experiments P2 and MAGIX in this chapter. The focus in this chapter is the MAGIX experiment since this work is contributing to it.

2.1 MESA - Mainz Energy-Recovering Superconducting Accelerator

The planned setup of the future facility MESA is shown in figure 2.1. The positions of the electron source (a), the two superconductive cavities (b), the P2 experiment (c) and the MAGIX experiment (d) are marked with red letters, respectively. The electron source STEAM (**S**mall **T**hermalized **E**lectron Source **A**t **M**ainz) will mainly consist of a UV (Ultra Violet) laser pointing on a photosensitive and semiconductive surface on a constant electric potential [Fri15, A⁺94]. The laser extracts electrons from the surface which are accelerated due to the electric potential of up to 200 kV. To get monoenergetic electrons from the source, it is crucial that the potential is low enough to prevent field emission. Further an ultra high vacuum (UHV, which is defined as a pressure of $p = 10^{-7} \text{ mar} - 10^{-14} \text{ mbar}$ [Ley07]) is needed to minimise scattering of the electrons. The

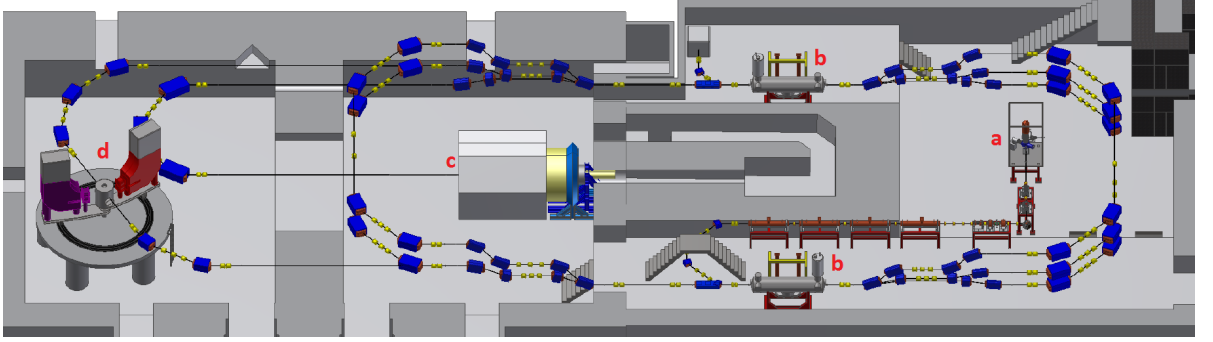


Figure 2.1 – Planned setup of MESA: The electron source is located at 'a', the two cavities at 'b', the P2 experiment at 'c' and the MAGIX experiment at 'd' [Rau16].

created electron beam will be guided by magnetic dipole fields into the pre-accelerator MAMBO (**MilliAM**pere **BO**oster). There will be two Wien filters (velocity filters) directly after the electron source. Wien filters consist of an electric and a magnetic field perpendicular to the electron velocity and to each other [Gel74]. Only neutral particles and charged particles with a velocity $v = \frac{E}{B}$ can pass the Wien filter, while all other charged particles leave the beam due to the Lorentz force. The electrons will be accelerated in the pre-accelerator MAMBO in four RF (Radio Frequency) cavities at room temperature to 5 MeV [H⁺15]. These RF cavities are build of multiple cells around the beam. The walls of these connected cells are conductive and on a high alternating voltage [Wei94]. The effect of this voltage is a standing wave (of a half wavelength) in each cell. The standing waves alternate in a way that every particle accelerated in the first cell passes over to the second cell during the electric field change, where the particle is then further accelerated. This concept continues through the whole cavity. Since the velocity of the particle is growing, the length of the cells is not constant, but shrinking. After MAMBO, the electrons will already be close to the speed of light ($\beta = 0.9957$). The pre-accelerated electrons will then be injected into the main accelerator with a frequency of 1.3 GHz, which is the frequency of the alternating voltage of MAMBO. The main accelerator is a linear accelerator, but built in circles in a way that the electrons will pass the two accelerating cavities up to three times. In principle, these cavities work the same as the RF cavities of MAMBO, but to get a higher field strength the whole cavity is superconductive [S⁺15]. This superconductivity is achieved by cooling down the cavities to 2 K by helium. Each of the two superconductive cavities consists of 9 cells, which gives a total length of around 3.5 m. Since the electrons are already close to the speed of light

in the main accelerator, the cells of the superconductive cavities are all of the same length. The cavities have a diameter of around 1 m. Every time an electron passes one of the two superconductive cavities it is accelerated by 25 MeV up to a maximal energy of 155 MeV. Dipole magnets will be used to keep the electrons on the accelerator path and quadrupole magnets will be used to keep the electron beam focused. Focusing a beam of charged particles by quadrupole magnets works over four stages (FODO) [RS92]. In the first stage the beam is focused (F) vertically but defocused horizontally by a quadrupole magnet. The second stage is some empty space (O) and the third stage is another quadrupole magnet turned by 90° according to the first quadrupole magnet. This second magnet focuses the beam horizontally but defocuses (D) it vertically. After the fourth stage, which is the second empty space (O), the beam is in total better focused vertically and horizontally.

MESA will be able to run in two modes: The extracted beam (EB) mode and the energy recovery linac (ERL) mode [Aul14]. In the EB mode the electron beam has to pass both cavities three times and will then be extracted with an electron energy of 155 MeV and a current of up to 0.15 mA to hit the external target of the beam dump experiment P2 (**P**recision experiment **2**). P2 is designed to measure the electroweak mixing angle or so called Weinberg angle θ_W , which is one of the fundamental parameters of the Standard Model. The Weinberg angle can be measured in various ways, but P2 is going to use elastic electron proton scattering with a low energy transfer. There is an asymmetry of the cross sections $\sigma_{L/R}$ for the different polarisations L/R [B⁺15]

$$A_{PV} = \frac{\sigma_L - \sigma_R}{\sigma_L + \sigma_R} = \frac{G_F Q^2}{4\sqrt{2}\pi\alpha} (Q_W + F(Q^2)) \quad (2.1.1)$$

where $F(Q^2)$ is the form factor of the proton for the squared four-momentum transfer Q^2 , α is the fine structure constant and G_F is the Fermi constant. For low Q^2 the contribution of the form factor is small. The asymmetry is then dominated by $Q_W = 1 - 4\sin^2\theta_W$. P2 will use different polarized beams from MESA to measure the elastic scattering cross sections of the electrons with a hydrogen target. The target is a cell filled with cooled hydrogen at around 16 K. Behind the target is a Solenoid-Spectrometer, a powerful magnet that bends incoming particles dependent on their energy

and absorbs bremsstrahlung and other background. The spectrometer leads to quartz gas coupled to Cherenkov detectors to detect the electrons using the spatial resolution to calculate the energy resolution. Further information on P2 can be found in [BGS16,B⁺15].

The ERL mode will be the special mode of MESA. In this mode the beam energy of 105 MeV is lower than in the EB mode, but the maximal current of 10 mA will be much higher due to the recovering of energy [Sim14]. The beam will be extracted after passing the cavities twice and guided to the **MESA Gas Internal Target EXperiment** (MAGIX). After interacting with the target, the beam will be returned to the accelerator with a phase shift of π caused by the path length. The returning beam is going to be decelerated by the superconductive cavities due to its phase shift. After two circulations, 100 MeV of the kinetic energy of the beam will be returned to the cavities. In this way the accelerator will be able to run with high currents but with a low need of energy which keeps the operation expenses low, too. The remaining beam is dumped at an energy of 5 MeV.

2.2 MAGIX - MESA Gas Internal Target EXperiment

The MAGIX experiment will be built at MESA for investigations on the proton radius and to search for dark photons [MAG16]. Two different experimental methods resulted in different values for the proton radius, being more than five times their uncertainties apart [Car15]. On the one hand there are measurements using electron proton scattering and the Lamb shift in electronic hydrogen which lead to a proton radius of $r_{p, \text{electronic}} = 0.8775(51)$ fm. On the other hand there are measurements on the Lamb shift in myonic hydrogen which lead to a proton radius of $r_{p, \text{myonic}} = 0.84087(39)$ fm [Car15]. Since all the systematics have been double-checked, this could be a hint for physics beyond the standard model. MAGIX is designed to measure the electromagnetic form factor of the proton by electron proton scattering with a higher precision to solve this disagreement. While dark photons can not be measured directly, their decay products can. According to popular theories, dark photons have properties similar to photons, thus they may decay into an electron-positron pair [B⁺09]. These electron-positron pairs

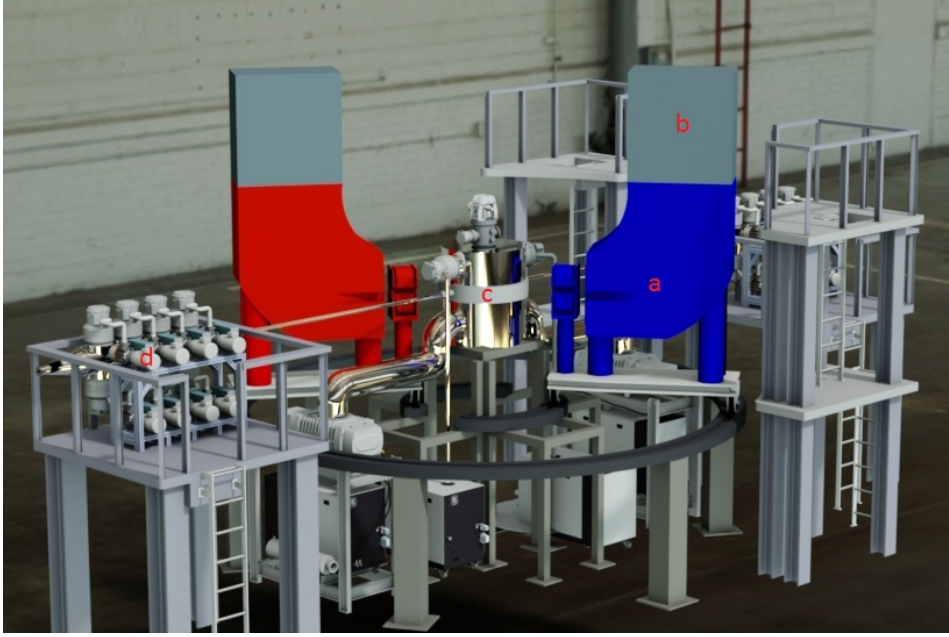


Figure 2.2 – Planned setup of MAGIX: At label 'a' are the two spectrometers with their GEM detectors at label 'b'. Label 'c' marks the scattering chamber with the internal gas target, while at label 'd' there are differential pumping sections in both directions along the beam pipe [MAG16], edited.

can be measured by MAGIX and the dark photon mass can be reconstructed.

MAGIX will consist of a gas target and two spectrometers, which will be rotatable around the vertex point. Two spectrometers are needed to measure the electron-positron pair from the decay of a dark photon simultaneously. Figure 2.2 shows a sketch of the planned setup of MAGIX. The incoming electron beam will have an energy of 105 MeV and a current of up to 10 mA. The target will be a gas-jet target perpendicular to the beam axis with an approximate areal density of $\rho_A \approx 10^{19} \text{ cm}^{-2}$ and a volume flow of $q_V = 40 \frac{\ell_n}{\text{min}}$, which is the performance limit for the vacuum pumps, the hydrogen purifier and the flow measuring devices. A detailed description of the gas target for MAGIX will follow in chapter 5. The origin of the gas-jet (a Laval nozzle) will be opposed by a catcher as shown in figure 2.3 to lead off the main part of the gas-jet. The distance between the nozzle and the catcher is designed to be only a few millimetres to improve the vacuum in the interaction chamber. On both sides of the gas target along the beam pipe will be differential pumping sections to keep the quality of the vacuum in the beam

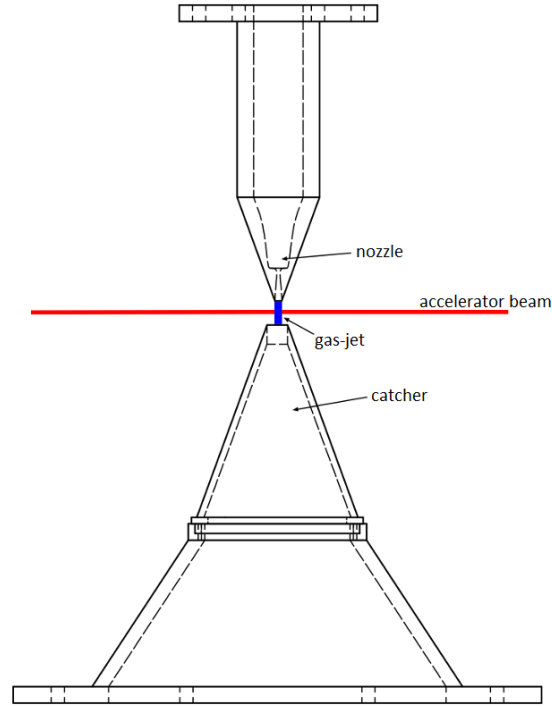


Figure 2.3 – Schematic sketch of the gas target for MAGIX [Rau16], edited. A catcher is opposed to the nozzle to improve the vacuum in the interaction chamber.

pipe high. The two spectrometers have been designed by Julian Müller [Mül14], their magnetic fields will bend any incoming charged particle dependent on its momentum and its incoming angle. The magnetic fields are designed in a way that every particle of the same momentum will reach the same point in the focal plane of the spectrometer. A simulation of the magnetic field in the spectrometers is shown in figure 2.4. In the focal plane will be GEM (Gas Electron Multiplier) detectors to amplify and measure the incoming particles. GEM detectors consist of an amplifying stage and a separate readout layer [Sau16]. The amplifying stage is a thin polymer foil clad in copper on both sides with a grid of holes in it. The holes are around $100\text{ }\mu\text{m}$ in diameter and distance to each other. The two copper layers are on a voltage of a couple of hundred volts. This generates high electric field strength in the holes. Incoming charged particles will create an electron avalanche in the holes. Behind the amplifying stage, the electrons drift towards the readout electronics which can be conductive stripes to get a spatial information, too. GEM detectors typically generate a gain of 10-100, but multiple layers can be used for higher gains. In MAGIX, GEM detectors are chosen for their speed due

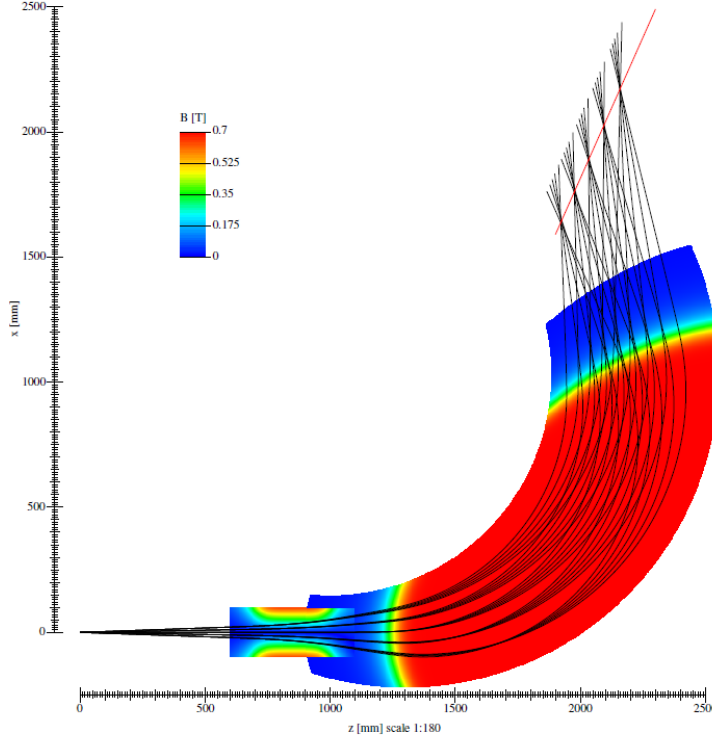


Figure 2.4 – Magnetic field in the spectrometer. The focal plane is marked with a red line. The particle trajectories (black lines) differ in momentum by $\Delta p = 10 \text{ MeV}$ or in the incoming angle by $\Delta\Theta = 2^\circ$ [Mül14].

to the separation of readout electronics and amplifying voltage, significantly reducing the issues caused by space charge. This is necessary for the high event rate MAGIX is aiming for. In combination with the spectrometer, the spatial resolution of the GEM detector corresponds to the momentum resolution. The detectors will reach a momentum resolution of $\frac{\Delta p}{p} = 6.881 \times 10^{-5}$ and an angle resolution of $\Delta\varphi = 0.0114^\circ$ [Mül14]. The angle φ is between the incoming electron beam and the current spectrometer position. These two spectrometers will be able to measure the momentum and the angle of particles scattered in the vertex point. MAGIX is aiming for a luminosity of $\mathcal{L} \approx 10^{35} \text{ cm}^{-2}\text{s}^{-1}$ to get significant signals of the rare decays of dark photons and good statistics for the measurements on the proton radius [MAG16].

3 Internal targets for fixed target experiments

Fixed target experiments are using one accelerated beam of particles and a fixed target instead of two colliding beams as collider experiments do. While collider experiments are able to reach much higher center of mass energies, fixed target experiments are able to reach higher luminosities [Eks95, B⁺13]. An internal target is a fixed target inserted directly in the beam pipe of an accelerator or storage ring. The beam passes the target multiple times and every beam particle that did not interact with the target particles remains in the accelerator or storage ring. Therefore, the accelerated beam is used more efficiently compared to an external target, since the beam is dumped after passing an external target once. The downside is that internal targets are limited in their density, because elastic scattering of the beam with the target decreases the beams intensity. A very dense target decreases the beam rapidly, losing it after a few transitions and the big advantage of an internal target is not utilized properly. Beam cooling mechanisms can cancel this effect up to a certain degree. This results in typical areal densities of $\rho_A = 10^{13} - 10^{16} \text{ cm}^{-2}$ for internal targets [Eks95] while higher densities up to e.g. $\rho_A = 10^{19} \text{ cm}^{-2}$ are possible. There are several different types of internal targets for fixed target experiments available: Gas-jets, cluster-jets, pellets and thin solids. MAGIX is going for a gas-jet target, because a very high density is needed to achieve the wanted luminosity and only gas-jets and thin solids are able to reach this high density. Due to the high beam currents of MESA solids would melt away, resulting in an unstable target. On account of this, the functionality of gas-jet and cluster-jet targets are described in this chapter.

3.1 Luminosity

MAGIX is aiming for a luminosity of $\mathcal{L} \approx 10^{35} \text{ cm}^{-2} \text{ s}^{-1}$ [MAG16]. The luminosity \mathcal{L} is defined as the ratio of the measured event rate \dot{N} and the cross section σ of the measured interaction [Wil96]

$$\dot{N} = \mathcal{L} \sigma . \quad (3.1.1)$$

For internal target experiments the luminosity can be written as the product of the beam particle current Φ_{beam} and the areal density of the target ρ_A [HM03]

$$\mathcal{L} = \Phi_{\text{beam}} \cdot \underbrace{\rho_{\text{target}} \cdot \ell}_{\rho_A} \quad (3.1.2)$$

while ρ_{target} is the volume particle density of the target and ℓ is the length of the target in beam direction.

The beam current of MESA using the ERL mode will be up to $I = 10 \text{ mA}$ [Sim14]. This equates to a particle current of $\Phi = I/e = 6.24 \times 10^{16} \text{ s}^{-1}$. Reaching the design luminosity of $\mathcal{L} \approx 10^{35} \text{ cm}^{-2} \text{ s}^{-1}$ [MAG16] required the areal density of the gas target to be at least $\rho_A = \frac{\mathcal{L}}{\Phi} \approx 1.6 \times 10^{18} \text{ cm}^{-2}$, according to formula 3.1.2. The design areal density of the target is set to the next order of magnitude $\rho_{A, \text{ design}} = 10^{19} \text{ cm}^{-2}$.

3.2 Supersonic gas-jet targets

Supersonic gas-jets are created by pressing gas through a Laval nozzle. A Laval nozzle consists of a convergent inlet and a divergent outlet with circular profiles. While passing a Laval nozzle, the velocity of the passing gas is greatly increased while temperature and pressure are decreased by adiabatic cooling [Mbu13]. The gas reaches sonic velocity c_{sonic} at the narrowest point of the nozzle and is accelerated further while leaving the nozzle through the divergent part. The profile of a Laval nozzle and the trends of velocity v ,

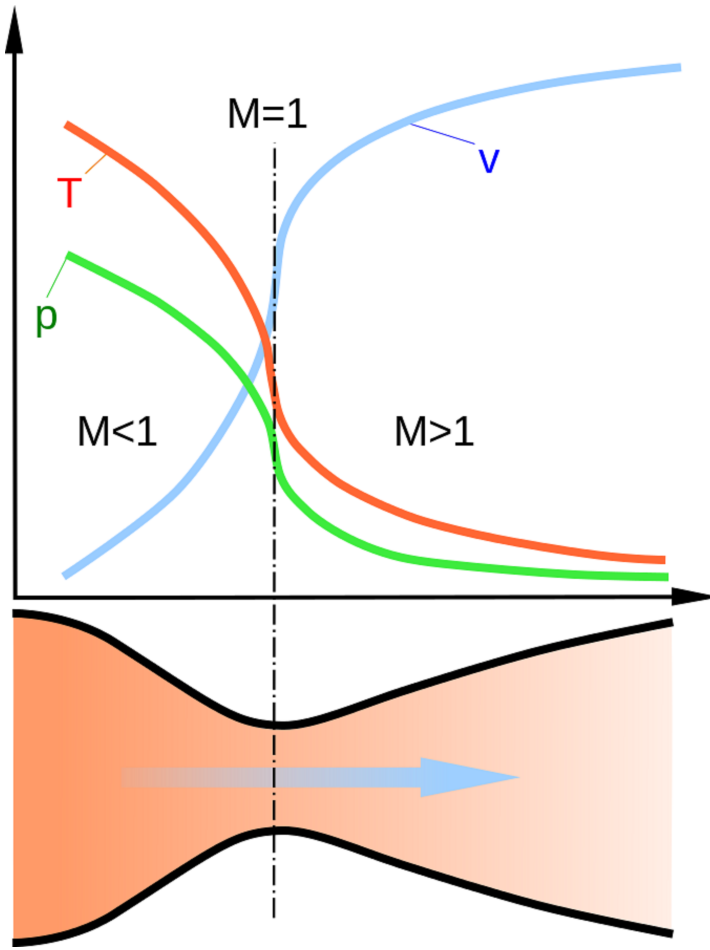


Figure 3.1 – Profile sketch of a Laval nozzle. The upper part shows the trends of temperature T , pressure p , velocity v and Mach number M of the gas passing the nozzle from left to right [Wik08].

Mach number $M = \frac{v}{c_{\text{sonic}}}$, temperature T and pressure p of the gas passing the Laval nozzle are shown in figure 3.1.

The process requires a high pressure difference between inlet and outlet of the nozzle. Since gas-jet targets are usually operated with an inlet pressure of $p_{\text{inlet}} > 5$ bar to reach a sufficiently high density and expand into the vacuum of the interaction chamber, the required pressure difference is already fulfilled. In case of internal gas- and cluster-jet targets, the gas is usually cooled to a temperature of around 40 K before passing the Laval nozzle [Eks95]. There may be orifices between the nozzle and interaction chamber to keep the background pressure low. Such a gas-jet target can be operated with many different gases like hydrogen, helium, deuterium, nitrogen or even xenon [R⁺97]. Dependent

on temperature, pressure and the gas type an areal density of up to 10^{18} cm^{-2} can be reached shortly behind the nozzle with internal gas-jet targets [Eks95]. Higher densities can be reached directly behind the nozzle. The density of a jet with constant divergence decreases with the distance from the nozzle $\rho_A \propto \frac{1}{r^2}$. Since the density of gas-jets decreases even faster due to the scattering with residual gas of the same mass as the gas particles, gas-jet targets are only a reasonable choice when the detector geometry allows a nozzle close to the beam. At certain inlet pressure and gas temperature combinations the gas target turns into a cluster-jet target with clusters of around 10^6 atoms.

4 Mach-Zehnder interferometer

The density profile $\rho_A(x, y, t)$ of a gas-jet can be measured with a Mach-Zehnder interferometer. The interference pattern shows an image of the invisible gas-jet. Even the development of a gas-jet over time can be measured by taking multiple pictures of the interference pattern in quick succession. The working principle of Mach-Zehnder interferometers and the connection between the measured interference pattern and the gas-jet density profile are described in this chapter.

4.1 Principle of Mach-Zehnder interferometers

As known from the photoelectric effect and the double-slit experiment, light behaves as a particle (photon) as well as an electromagnetic wave [Sch13]. The alternating electric and magnetic fields of an electromagnetic wave are perpendicular to each other and to the direction of propagation. Since the electric \vec{E} and the magnetic \vec{B} fields are in phase [Mes09], only one of them is needed to describe the light wave

$$E(\vec{r}) = |E| e^{i(\vec{k} \cdot \vec{r} - \omega t + \Phi)} \quad (4.1.1)$$

with the electric field strength $E(\vec{r})$ at the position \vec{r} , the maximal electric field strength $|E|$, the wave vector \vec{k} , the angular frequency of the wave ω and the phase Φ .

The best light source for any interferometer is a laser (light **a**mplification by **s**timulated **e**mission of **r**adiation), because interference needs coherent light, which is provided by a laser [KS08]. A coherent light source emits light with a large coherence length, which

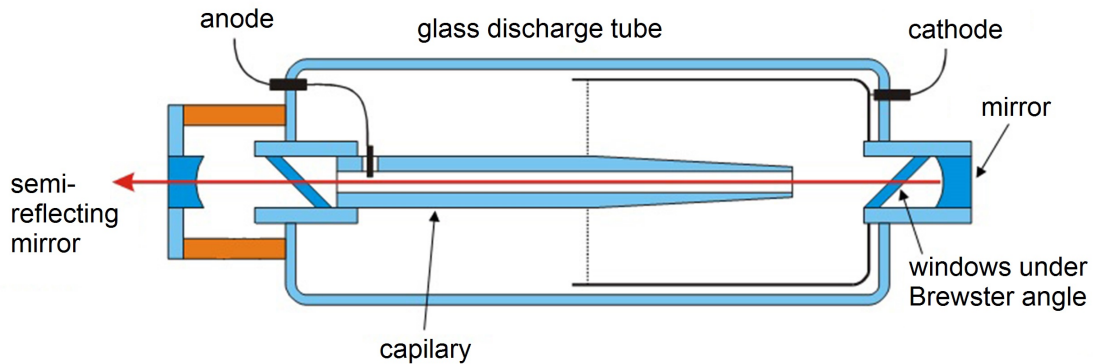


Figure 4.1 – Sketch of a Helium-Neon-Laser [Laz], edited. The Helium-Neon gas in the capillary tube is excited by an electric discharge between anode and cathode. The two mirrors reflect the laser back into the medium causing stimulated emission and light amplification. The laser beam is emitted through the semi-reflecting mirror at the left side.

is the average distance between two successive phase shifts. Stabilised lasers have a coherence length of up to 5 km [KS08].

In this work a Helium-Neon-Laser, one of many different laser types, is used: Therefore, the working principle of lasers is not described in general, but in the specific case of HeNe-Lasers. HeNe-Lasers consist of a capillary tube with a typical length of 10 cm and a typical diameter of 1 cm filled with a gas mixture of Helium and Neon in a ratio of approximately 10:1 [Mes09, KS08]. A schematic diagram of the capillary tube is shown in figure 4.1. It has mirrors on both end caps, one with a reflectance of 99.9% and one with a reflectance of 99%. The helium atoms are the pumping medium, they are getting excited from the ground state to the 2^1S_0 and the 2^3S_1 states by an electric discharge caused by 7 – 8 kV between anode and cathode (cf. figure 4.1). A sketch of all involved energy levels of helium and neon is shown in figure 4.2. The excited helium atoms transfer their excitation energy to neon atoms (the laser medium) by inelastic collisions. In these collisions the helium atoms return to the ground state and neon atoms are raised from the ground state to the $3s$ or the $2s$ states which are very close to the two excited helium states. Since there are a lot more helium atoms than neon atoms, this mechanism leads to a population inversion for the neon atoms. There are more excited neon atoms than ground state neon atoms. The excited neon states go over to $3p$ and $2p$ states emitting

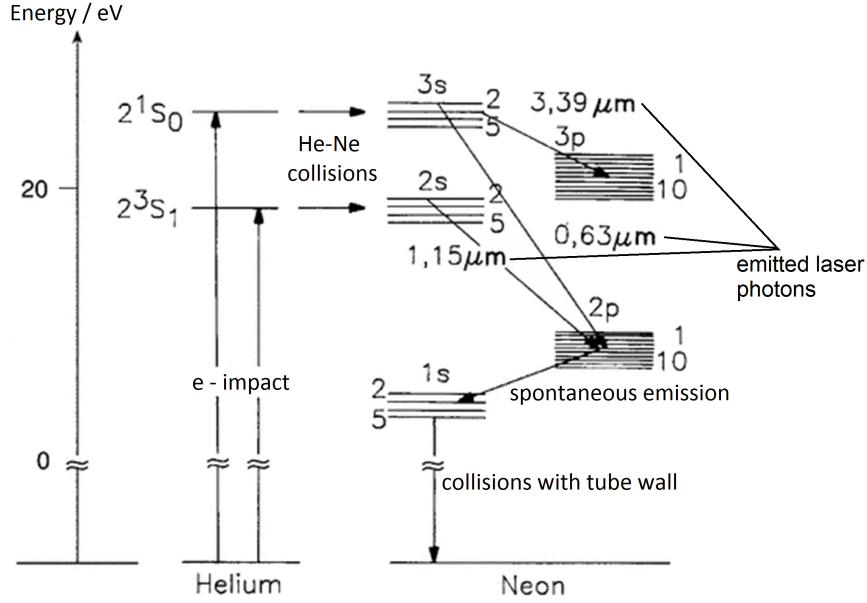


Figure 4.2 – Diagram of the involved energy levels of helium and neon in a HeNe-Laser [EE15], edited. The helium atoms get excited by an electric discharge and transfer their excitation energy to neon atoms by inelastic collisions. This causes a population inversion for the neon atoms, which go from the 3s or 2s to the 3p or 2p states while emitting the laser photons.

the laser photons. The p states have very short lifetimes of $\tau_p \approx 10$ ns [KS08] and go further to the 1s state from where the atoms go to the ground state by collisions with the wall of the capillary tube and by spontaneous emission. The mirrors at the end caps of the tube reflect the laser light from the neon 3s to 2p transition back into the medium causing a stimulated emission of the still overpopulated 3s neon state. This mechanism is called light amplification. One of the mirrors at the end caps of the capillary tube has a reflectance of 99%, that means 1% of the produced light is emitted as the laser beam. Many lasers have Brewster mirrors in front of the end-cap mirrors to emit only light of a single polarisation. The emitted laser light is monochromatic ($\lambda = 632.8$ nm), linear polarised and has a large coherence length.

In Mach-Zehnder interferometers a laser beam is split by a beam splitter into two parts with equal intensity but different propagation directions. These two beams can be reunited at another beam splitter, causing interference. Assuming the same propagation direction \vec{e}_z , the same path length z and the same propagation time t for both beams,

this results in adding up the electric fields from formula 4.1.1 of both beam parts

$$E_1(z, t) + E_2(z, t) = \underbrace{(|E_1| e^{i\Phi_1} + |E_2| e^{i\Phi_2})}_{|E_{\text{total}}|} e^{i(k_z z - \omega t)}. \quad (4.1.2)$$

The light intensity I is [Sch13]

$$I \propto |E_{\text{total}}|^2 = (|E_1| e^{i\Phi_1} + |E_2| e^{i\Phi_2}) (|E_1| e^{-i\Phi_1} + |E_2| e^{-i\Phi_2}) \quad (4.1.3)$$

$$= |E_1|^2 + |E_2|^2 + 2|E_1||E_2| \cos \Delta\Phi \quad (4.1.4)$$

$$\Rightarrow I = I_1 + I_2 + 2\sqrt{I_1 I_2} \cos \Delta\Phi \quad (4.1.5)$$

with the phase difference $\Delta\Phi = \Phi_1 - \Phi_2$ and using $e^{ix} - e^{-ix} = 2 \cos x$. The interference effect can be seen in the last term of the intensity of the two superposed beams. Maximal constructive interference accords to maximal intensity, which is given at $\cos \Delta\Phi = 1$ or $\Delta\Phi = 0$ while maximal destructive interference accords to a minimal intensity at $\cos \Delta\Phi = -1$ or $\Delta\Phi = \pi$. For the interference of two beams of equal intensity the maximal destructive interference intensity is vanishing $I(\Delta\Phi = \pi) = 0$.

In the setup of one split and then reunited laser beam, the two beams interfere constructively. But if one of the beams is delayed by a slightly longer path or by a medium in its path, an interference pattern with constructive and destructive interference is achieved. This is called an optical path difference $\Delta L = L_1 - L_2$ which is the difference of the optical path lengths calculated by the product of the geometrical path s and the refractive index n [Dem09]

$$L = n \cdot s. \quad (4.1.6)$$

Assuming that only one of the beams is slowed by a different refractive index Δn in a defined region, the optical path difference can be rewritten as a phase difference

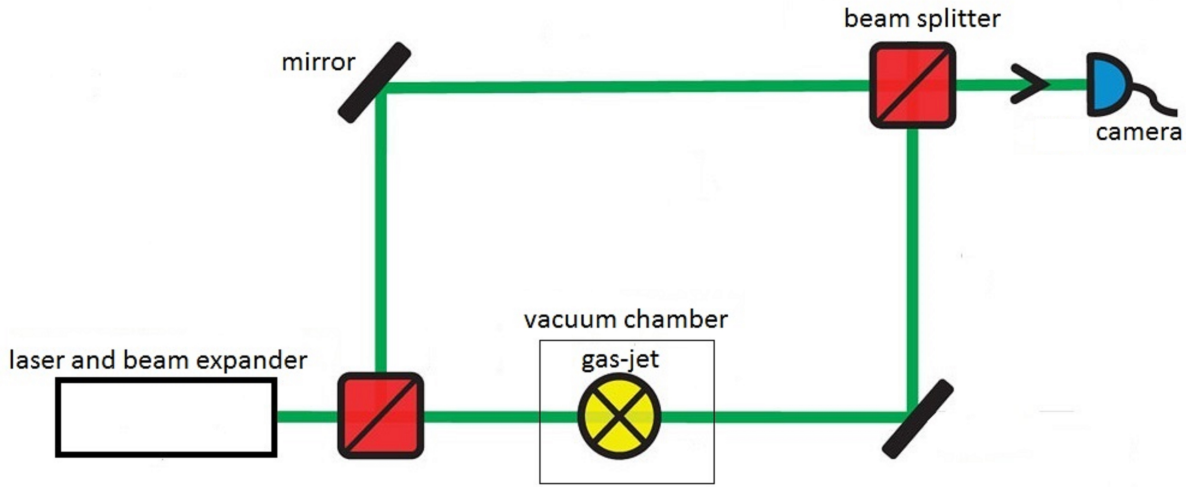


Figure 4.3 – Sketch of a Mach-Zehnder interferometer [Z⁺11], edited. The laser beam is expanded and split into two equal beams. One beam passes the vacuum chamber and the gas-jet before it is reunited with the other beam, which is just redirected to the beam splitter. A camera takes a photo of the interference pattern of the superposed beams.

between the two beams as long as the optical path difference is lower than the coherence length [M⁺00]

$$\Delta\Phi = \frac{2\pi}{\lambda} \int \Delta n \, dz \quad (4.1.7)$$

with the direction of the beam \vec{e}_z .

Exactly this is used in a Mach-Zehnder interferometer. The setup of a Mach-Zehnder interferometer is shown in figure 4.3. A laser beam is expanded and then split up by a beam splitter into two beams of equal intensity. One of the beams (the reference beam) is redirected by a mirror to the second beam splitter where it is reunited with the other beam (the test beam), which is not only redirected by the second mirror towards the second beam splitter, but also passes a test medium. The medium can be a chamber filled with gas, a candle or flowing gas for example. In this work the interferometer is used to investigate the characteristics of gas-jets.

The gas-jet as the test medium has a refraction index slightly different to the refraction index of the air, due to its different density. The relation between density ρ of a gas and its refraction index is given by the Gladstone-Dale relation [SV12]

$$\frac{\Delta n}{\rho} = \frac{n - 1}{\rho} = k_{\text{GD}} = \text{constant} \quad (4.1.8)$$

with the Gladstone-Dale constant k_{GD} . Formula 4.1.7 can be rewritten with the Gladstone-Dale relation to

$$\Delta\Phi = \frac{2\pi}{\lambda} \int \Delta n \, dz \quad (4.1.9)$$

$$= \frac{2\pi k_{\text{GD}}}{\lambda} \int \rho \, dz \quad (4.1.10)$$

and the areal density of the gas-jet in beam direction ρ_{A} can be introduced to get

$$\rho_{\text{A}} = \int \rho \, dz = \frac{\Delta\Phi \lambda}{2\pi k_{\text{GD}}} . \quad (4.1.11)$$

The areal density ρ_{A} is proportional to the phase difference $\Delta\Phi$ between the two beams.

Figure 4.4 shows an interference pattern measured with a Mach-Zehnder interferometer. The constant phase shift between the two laser beams is shown by the parallel interference fringes. The shadow of the nozzle is centred in the lower region of the image. The effect of the gas-jet on the interference pattern is visible above the center of the nozzle. The interference fringes are shifted there by a phase difference.

An alternative evaluation of the interference pattern uses the assumption of a cylindrical symmetry of the gas-jet, based on the cylindrical symmetry of the nozzle. Figure 4.5 shows a top view of the gas-jet with the direction of the laser beam \vec{e}_z , the direction

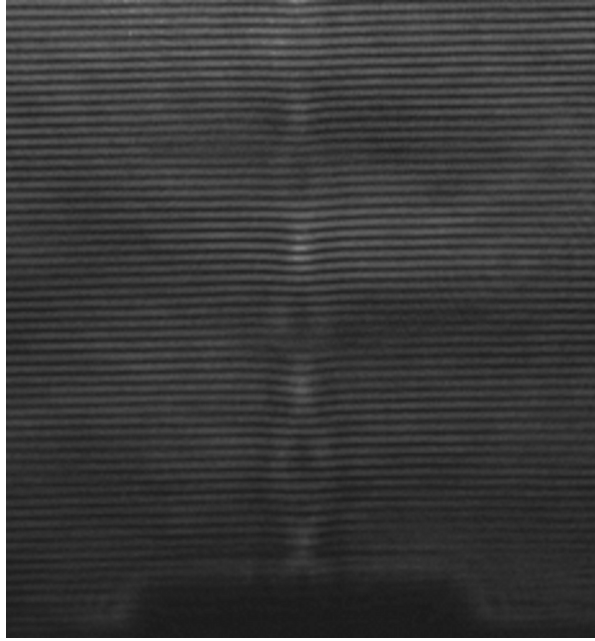


Figure 4.4 – Interference pattern of a Mach-Zehnder interferometer taken with a CCD camera. The parallel fringes show a constant phase-difference between the two laser beams for a wide area. The shadow of the nozzle is at the bottom of the image. A shift in the interference fringes can be seen above the center of the shadow of the nozzle. This is the effect of the gas-jet.

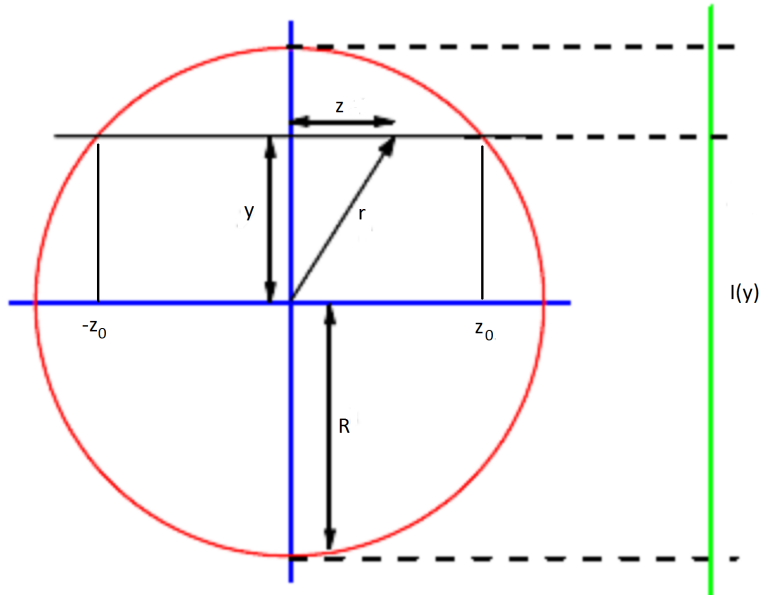


Figure 4.5 – Sketch of the laser beam passing the gas-jet (red circle) from left to right [LHH07], edited. The gas-jet is pointing out of the plane of projection. The intensity $I(y)$ contains the phase difference caused by the gas-jet, which can be made visible by interference with the reference beam, resulting in an interference pattern as shown in figure 4.4.

of the gas-jet \vec{e}_x (out of the plane of projection) and the direction \vec{e}_y perpendicular to \vec{e}_x and \vec{e}_z . The phase difference from formula 4.1.7 can be transformed to cylindrical coordinates

$$\Delta\Phi(x, y) = \frac{2\pi}{\lambda} \int \Delta n(x, y, z) dz \quad (4.1.12)$$

$$= \frac{4\pi}{\lambda} \int_y^{R_x} \frac{r \Delta n(x, r)}{\sqrt{r^2 - y^2}} dr \quad (4.1.13)$$

$$= \frac{4\pi k_{\text{GD}}}{\lambda} \int_y^{R_x} \frac{r \rho(x, r)}{\sqrt{r^2 - y^2}} dr \quad (4.1.14)$$

with $r^2 = y^2 + z^2$ and the radius of the gas-jet R_x at the height x . Solving this integral is possible by using an Abel transform or by assuming the shape of the density (F-Interpolation). A good assumption for the density is a Gaussian distribution for every height x above the nozzle

$$\rho_x(r) = a_x e^{-\frac{r^2}{b_x^2}} \quad (4.1.15)$$

with unknown amplitude parameter a_x and the unknown width parameter b_x and the distance from the center of the nozzle in \vec{e}_y direction r . This ansatz can be plugged into equation 4.1.14 and the integral can then be solved [F⁺11]

$$\Delta\Phi_x(y) = \frac{4\pi k_{\text{GD}} a_x}{\lambda} \int_y^{R_x} \frac{r e^{-\frac{r^2}{b_x^2}}}{\sqrt{r^2 - y^2}} dr \quad (4.1.16)$$

$$= \frac{\pi \sqrt{\pi} k_{\text{GD}}}{\lambda} a_x b_x e^{-\frac{y^2}{b_x^2}} \operatorname{erf} \left(\frac{\sqrt{R_x^2 - y^2}}{b_x} \right). \quad (4.1.17)$$

For the determination of the phase shifts $\Delta\Phi(x, y)$ from the interference patterns, the two dimensional Fourier Transformation can be used.

4.2 Fourier Transformation

Every real-valued function $f(t)$ can be written as an infinite sum of trigonometric functions with different frequencies ω , because these trigonometric functions are building an orthonormal basis [FB08]

$$f(t) = \sum_{\omega=0}^{\infty} M_{\omega} \sin(\omega t + \Phi_{\omega}) \quad (4.2.1)$$

with the magnitudes M_{ω} and the phases Φ_{ω} , which can be calculated

$$\text{Magnitude: } M = \sqrt{\text{Re}(F)^2 + \text{Im}(F)^2} \quad (4.2.2)$$

$$\text{Phase: } \Phi = \arctan\left(\frac{\text{Im}(F)}{\text{Re}(F)}\right) \quad (4.2.3)$$

from the Fourier Transformation of the original function [FB08]

$$F(\omega) = \int_{-\infty}^{+\infty} f(t) e^{-i2\pi\omega t} dt. \quad (4.2.4)$$

While the magnitude gives a measure for the contribution of a single frequency to the original function, the phase is the shift of the trigonometric function of a single frequency. In most applications of the Fourier Transformation only the magnitude is used. But in this work it is used to calculate the phase shift from a diffraction pattern. For a discrete two dimensional function $f(i, j)$, like a greyscale image, the two dimensional discrete Fourier Transformation [RKH10]

$$F(k, \ell) = \sum_{i=0}^{N-1} \sum_{j=0}^{N-1} f(i, j) e^{-i2\pi\left(\frac{ki}{N} + \frac{\ell j}{N}\right)} \quad (4.2.5)$$

is used. Figure 4.6 and figure 4.7 show some examples for two dimensional sin waves with different frequencies or different directions with their magnitude images, respectively. The frequency axes are in the centre of the magnitude images. A sharp peak at the frequency of the particular sin wave and another at the negative frequency can be seen. The axis built by this two frequencies is parallel to the propagation direction of the sin wave.

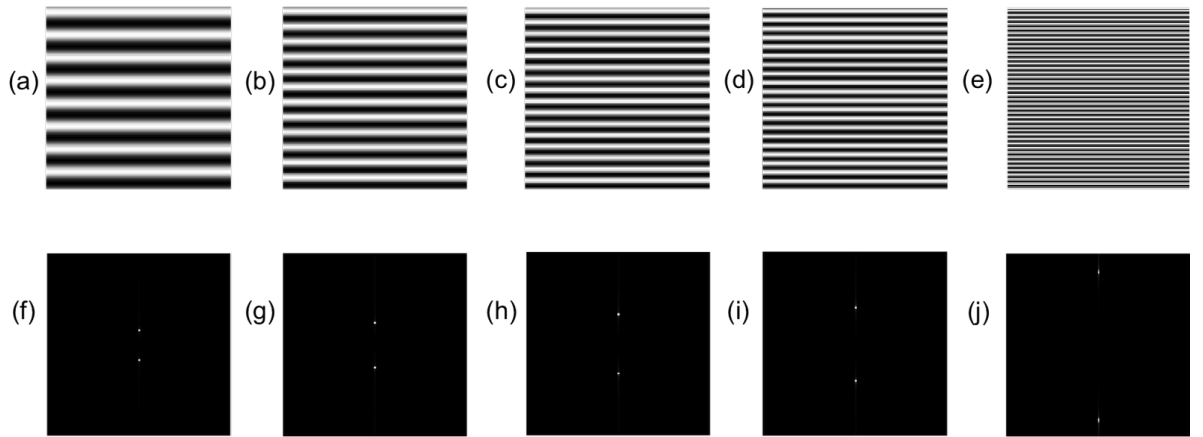


Figure 4.6 – Some examples of sin waves with different frequencies (a-e) and their magnitude images (f-j), respectively [Che11].

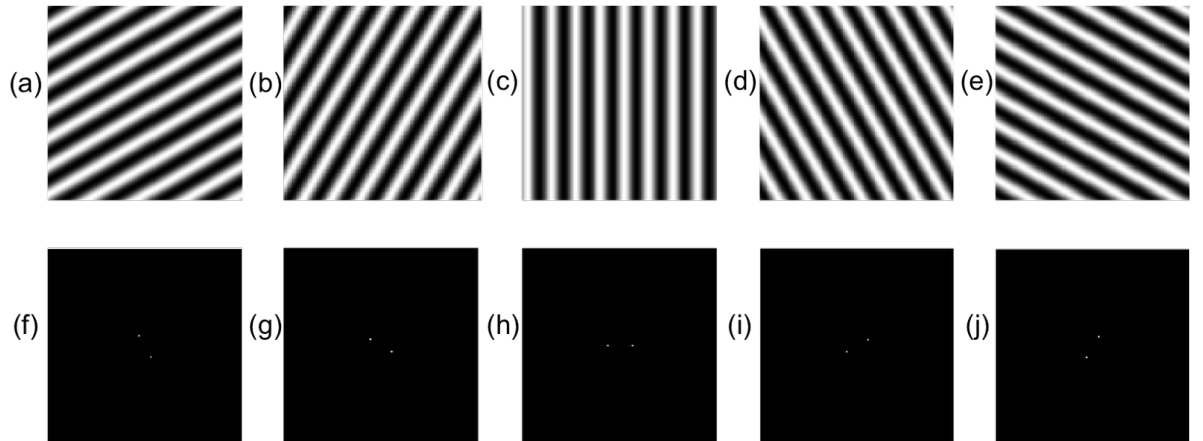


Figure 4.7 – Some examples of sin waves with different directions (a-e) and their magnitude images (f-j), respectively [Che11].

5 The experimental setup

The experimental setup consists of two parts. The gas-jet target for MAGIX and a Mach-Zehnder interferometer (s. section 4.1). The gas-jet target has been designed by Daniel Bonaventura and was built up by Daniel Bonaventura and Catharina Hargens (s. [Har16]) while the interferometer has been build up and tested by Christina Westphälinger on an optical table (s. [Wes16]). She optimised the optical elements and got a clear interference pattern with a high contrast. At the end of her work, the interferometer was able to visualise the effect of a gas-jet in the test beam. Combining both parts enables measurements of the density profile of the gas-jet target for MAGIX. In this chapter the launching of the gas-jet target and the rebuilding and optimisation of the Mach-Zehnder interferometer around the gas-jet target are described.

5.1 Building the experimental setup

The gas-jet target for MAGIX MCT-M (Münsteraner Cluster-Jet Target-MAGIX) will be a supersonic gas-jet target as described in chapter 3.2. A detailed CAD drawing of the final target for MAGIX is shown in figure 5.1. The quadratic vacuum chamber is at the same position as the interaction chamber will be as soon as the target is installed at MESA. The main parts of the target are the coldhead and the Laval nozzle. The coldhead (Leybold COOLPOWER 10 MD) uses a high pressure helium circuit, that is compressed in a compressor (Leybold COOLPAK 6000H) and expands in the coldhead, to cool down the gas flow in two stages, the warm and the cold stage. Both stages are equipped with heating elements and temperature measuring devices. The gas pipe is coiled around the cooling elements of the warm and the cold stage and leads to the nozzle afterwards. The gas pipe is made of copper in the region of the cooling stages and of stainless steel in

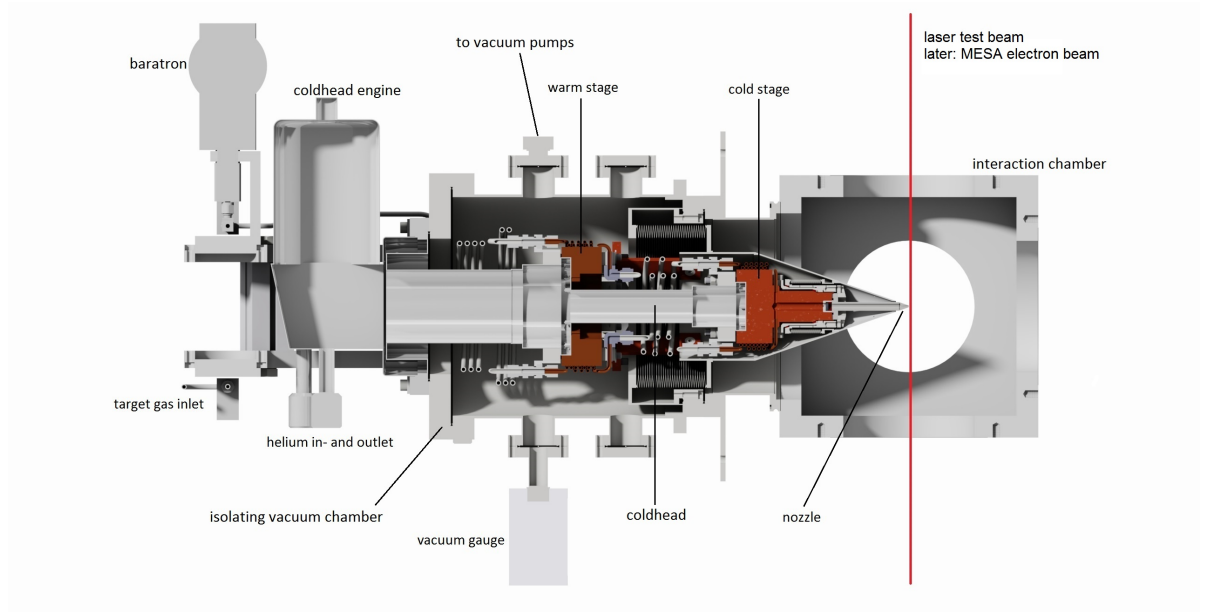


Figure 5.1 – CAD profile of the gas target for MAGIX (generated by Daniel Bonaventura, edited). The target gas enters the target on the bottom left side of the image and circuits around the warm and the cold stage of the coldhead until it gets through the nozzle and expands into the vacuum of the interaction chamber. A high pressure helium circuit is connected to the coldhead on the bottom. The helium expands in the coldhead and cools down the warm and the cold stage. A vacuum pump providing the isolating vacuum is connected at the top.

between, because the thermal conductivity of copper at temperatures of $10 - 100$ K is in the order of $\kappa_{\text{Cu}} \approx 10^3 \frac{\text{W}}{\text{mK}}$, while the thermal conductivity of stainless steel at the same temperature is in the order of $\kappa_{\text{steel}} \approx 1 - 10 \frac{\text{W}}{\text{mK}}$, a lot lower than copper [Täs12,MLR]. For a better isolation the coldhead is inside of an isolating vacuum chamber at a pressure of around 10^{-7} mbar. This results in an optimal cooling of the gas in the cooling regions and decreases the re-heating of the gas between the two cooling stages. The MCT-M has no orifices in the jet beam since the nozzle will be directly next to the electron beam of MESA.

After Catharina Hargens tests on the coldhead [Har16] for the target, the final testing setup has been built. It is shown in figure 5.2 and the main components of the target are marked. The compressor (a) provides compressed helium for the coldhead (b). The target gas flow passes a flow measuring device (c) and entering the coldhead from the bottom. A pumping station (d) creates the isolating vacuum around the coldhead and another pumping station (e) creates the vacuum in the interaction chamber (f). Since the estimated gas

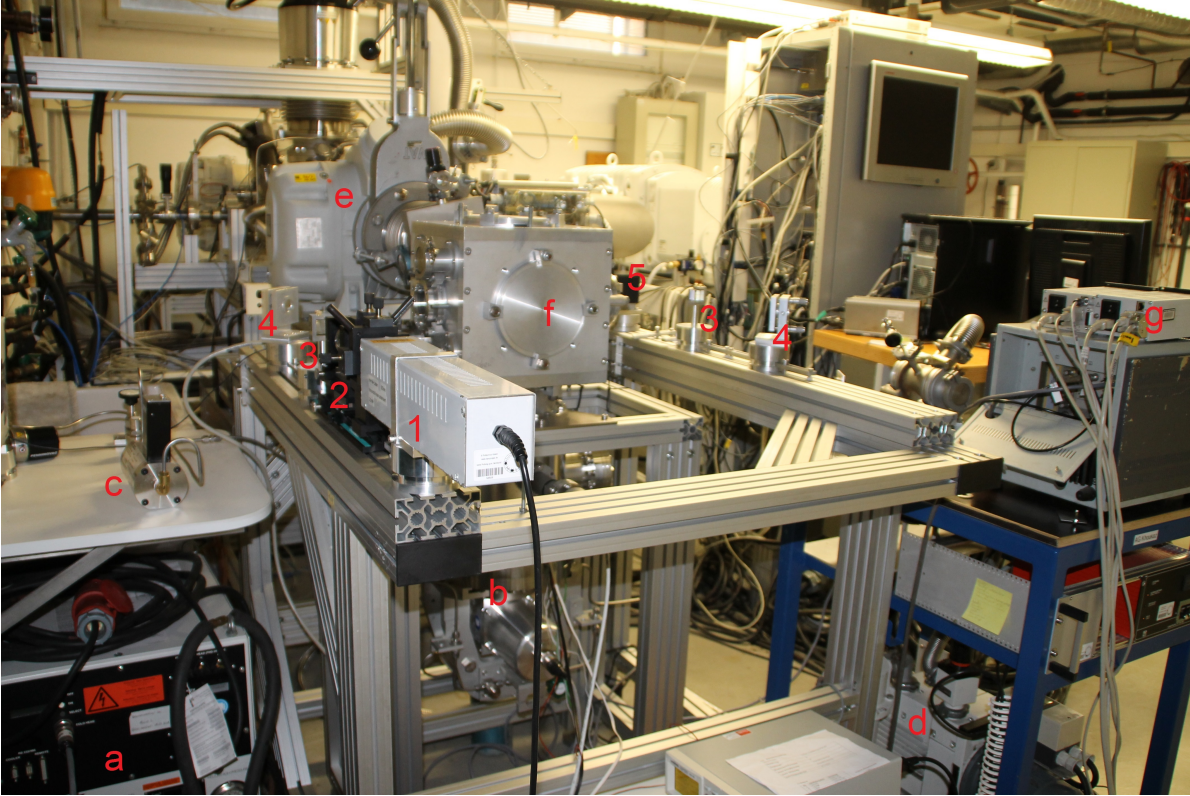


Figure 5.2 – A photography of the experimental setup. The main components of the gas-jet target are marked with red letters: The compressor (a), the coldhead (b), the flow measuring device (c), the two pumping stations (d + e), the interaction chamber (f) and the vacuum monitors (g). The gas-jet is from bottom to top in the interaction chamber. The Mach-Zehnder interferometer is build on an own frame around the target. The components of the interferometer are marked with red numbers: The laser (1), the beam expander (2), the beam splitter cubes (3), the mirrors (4) and the camera (5). The camera is missing in the photo, because it was used to take it.

flow is around $40 \frac{\ell_n}{\text{min}}$, the pumping power for the interaction chamber can be increased by the $\overline{\text{P}}\text{ANDA}$ (Anti-Proton ANnihilation at DArmstadt) prototype pumping station in the background of the picture. The isolating vacuum and the vacuum in the interaction chamber are monitored (g) and the temperature of the warm and the cold stage of the coldhead can be monitored by a LABVIEW program written by Robin Balske (s. [Bal17]).

The nozzle at the top of the coldhead (cf. figure 5.1) has been designed by Stephan Aulenbacher (Johannes Gutenberg-Universität Mainz) and was build by Speedpart GmbH using laser sintering. The narrowest diameter of the nozzle is $350 \mu\text{m}$ and the outlet has

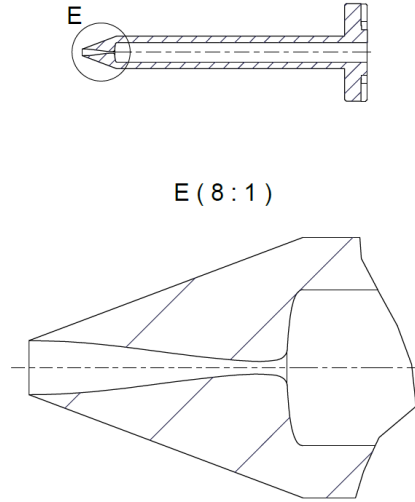


Figure 5.3 – Lateral cut of the used nozzle. The upper part shows the whole element and the lower part shows enlarged the convergent and divergent nozzle area. The gas flow is from right to left. Generated by Stephan Aulenbacher, edited by Daniel Bonaventura.

a diameter of 2000 μm . Figure 5.3 shows a lateral cut of the nozzle (not to scale).

A cubic vacuum chamber has been prepared as interaction chamber (cf. figure 5.1). It will be used just in this testing setup. The outlet of the nozzle of the target is supposed to be exactly in the middle of this chamber. Two windows are needed for the laser (test) beam. They have been made of acrylic glass and added to the chamber as blind flanges (cf. figure 5.1 at the top and the bottom of the interaction chamber). The whole chamber has been leakage tested with a helium leakage tester by evacuating the vacuum chamber and spraying helium on all seals. Any leak allows the helium to enter the vacuum chamber due to the pressure difference. The helium is then detected by the leakage tester. The leakage test is very important, because the target will amongst other gases be operated with hydrogen, which builds the explosive oxyhydrogen with oxygen from the air. Oxyhydrogen is explosive as long as the volume percentage of hydrogen is between 4 vol% and 77 vol% [JS13]. To prevent this, the leakage rate of the vacuum chamber needs to be lower than one fourth of the standby gas flow of the target. The measured leakage rates are around $(p\dot{V}) = 10^{-6} \frac{\text{mbar} \cdot \ell}{\text{s}}$ with the pressure p and the volume V . The minimal standby hydrogen flow Q_{H_2} needed for a save operation can be calculated from the leakage oxygen flow Q_{O_2} to

$$Q_{\text{O}_2} = \varphi_{\text{O}_2} \dot{n} V_{\text{m}} = \varphi_{\text{O}_2} \frac{(p\dot{V})}{RT} V_{\text{m}} \quad (5.1.1)$$

$$Q_{\text{H}_2} \geq 4 \cdot Q_{\text{O}_2} \quad (5.1.2)$$

$$\geq 4 \cdot 10^{-9} \frac{\ell}{\text{s}} \quad (5.1.3)$$

with the oxygen volume share of air φ_{O_2} , the amount of substance n , the molar volume V_{m} , the temperature T and the gas constant R . Since there will be a standby gas flow of around $10^{-3} \frac{\ell}{\text{s}}$ to prevent the blockage of the nozzle by frozen particles, the building of oxyhydrogen in the interaction chamber will not be a danger while operating the target.

After Christina Westphälinger tests on the Mach-Zehnder interferometer on an optical table, it has been rebuilt on an own KANYA aluminium frame (s. figure 5.2) around the target. There was no possibility to add the target to the optical table. The interferometer got its own frame to be decoupled from the target, because the coldhead and the vacuum pumps are causing vibrations. Transferring this vibration to the interferometer would destroy the interference pattern. The optical components can be fixed on the KANYA frame by stepless variable screw threads in the gaps. The gaps in the frame are helping a lot for the pre adjustment, but a well defined lattice of threads would do better. Some distance marks have been added on the KANYA frame for the pre adjustment. In this way it is much easier to build a rectangular with the two mirrors and the two beam splitters. Once every component is on the right spot, the fine adjustment starts. At first mirrors with a reflectivity of 50% have been used as beam splitters, because they are adjustable in the vertical and horizontal and they do not block the direction of the second interference pattern. For the fine adjustment the two laser dots on the screen in front of the camera have to be brought onto one spot and simultaneously the two laser dots in the other direction have to be superposed at a different distance from the beam splitter. This results in a parallel superposition of the two laser beams. Once this is done, the beam expander is added to the interferometer and again everything is fine adjusted until the camera shows an interference pattern. As soon as an interference pattern is visible, the beam splitters are exchanged one by one to beam splitter cubes to improve the quality of the interference pattern (cf. [Wes16]).

5.2 Optimisation of the Mach-Zehnder interferometer

The beam expander of the interferometer has been changed to improve the quality of images of the interference pattern. Christina Westphlinger [Wes16] used a simple beam expander consisting of a focusing and a collimating lens in one telescope, but it caused some relics in the beam profile. That was no problem for testing the interferometer in principle, but the relics of the beam expander often cause more relics in the reconstructed area density profile. An example for this is shown in figure 5.4.

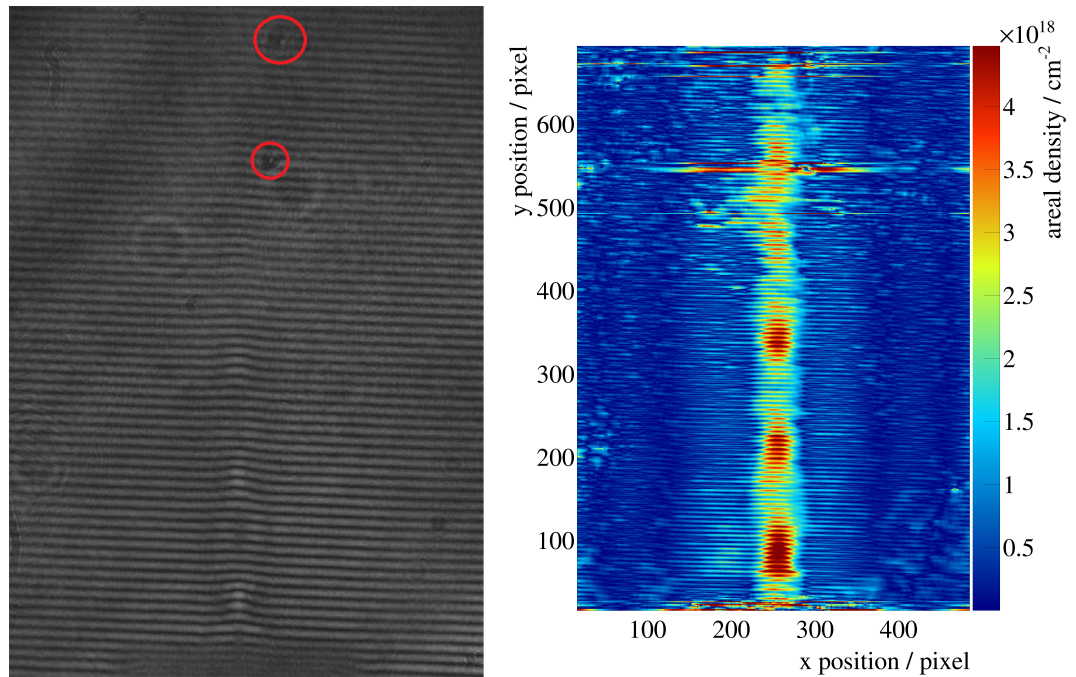


Figure 5.4 – On the left side is the interference pattern with some marked relics (taken by Christina Westphlinger). On the right side is the reconstructed area density profile with some errors in the spots corresponding to the relics in the interference pattern. The gas used is nitrogen, expanding into room pressure at room temperature with a pressure in front of the nozzle of $p_0 = 10$ bar.

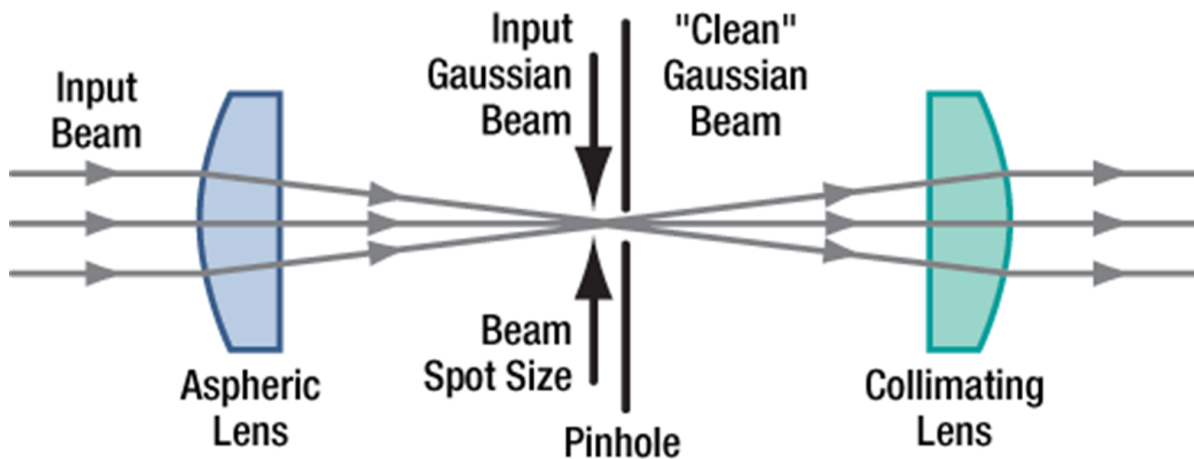


Figure 5.5 – Sketch of a spatial filter [Tho99]. The incoming laser beam is focused through a pinhole and collimated by the collimating lens. The expansion factor can be changed by adjusting the distance between pinhole and collimating lens.

To get rid of these relics in the beam profile, the beam expander has been substituted with a spatial filter. Christina Westphälinger [Wes16] already tested this. Spatial filters consist of a focusing lens (or a microscope objective), a pinhole and a collimating lens. The schematic setup of a spatial filter is shown in figure 5.5. The focusing lens focuses the laser, which has a diameter of approximately 1 mm, in its focal point where the pinhole with a diameter of $15\text{ }\mu\text{m}$ cuts off every component of the laser that is not focused in the focal point. This works like an analogue low pass. The Gaussian laser profile in front of the spatial filter and at the height of the pinhole are shown in figure 5.6. The noise is not focused through the pinhole, but cut away. The collimating lens is placed behind the pinhole to collimate the filtered laser for the interferometer. The distance of the collimating lens to the pinhole and its focal length fix the widening of the laser beam. In this setup a lens with a focal length of 10 cm is used to get a beam diameter of approximately 2 cm behind the spatial filter. The effect of the spatial filter on the laser beam is shown in figure 5.7. A definite improvement of the beam quality can be seen.

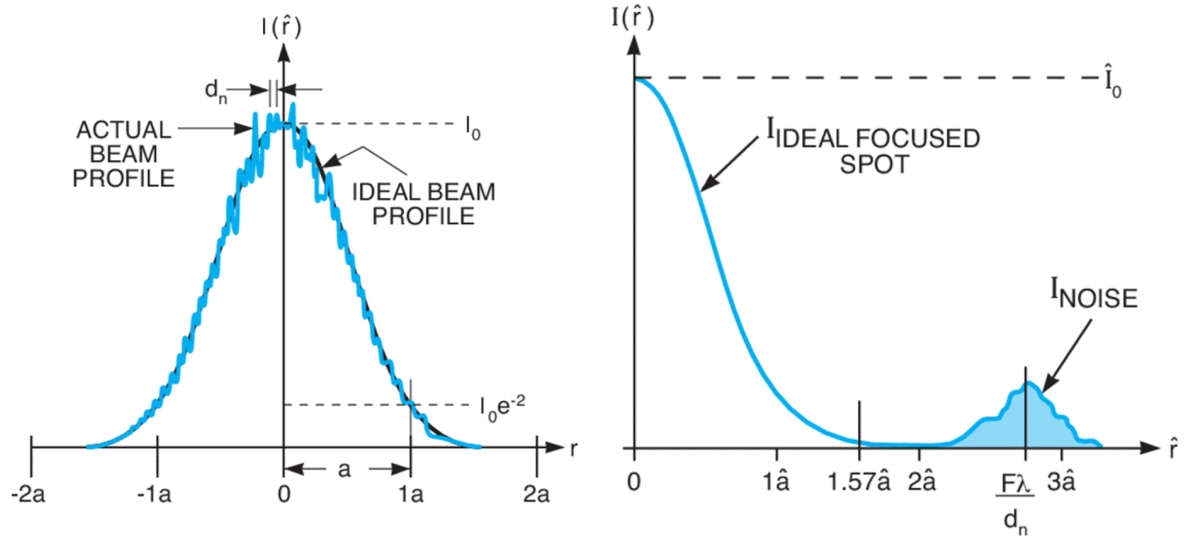


Figure 5.6 – On the left side is a Gaussian laser profile shown with noise [Np116]. The right side shows the laser profile on the height of the pinhole [Np116]. Using a pinhole with a radius of $2\hat{a}$ cuts away the noise without reducing the intensity of the Gaussian beam.



Figure 5.7 – Two laser beam profiles: On the left side with the old simple beam expander and on the right side with a spatial filter. Pictured in both images is an eyelash on the CCD camera. One sees a clearer beam profile on the right side even though some relics stay.

6 Density determination program

Measurements with a Mach-Zehnder interferometer result in an image of interference patterns such as the one shown in figure 6.1. In these patterns, the effect of a gas-jet in the test beam can be seen as a local displacement of the interference fringes. The local phase shifts $\Delta\Phi(x, y)$ caused by the gas-jet can be calculated from the interference pattern. These phase shifts are proportional to the areal density of the gas-jet (cf. formula 4.1.11) or can be used to calculate the volume density by F-interpolation (cf. formula 4.1.17). In this chapter two C++ programs are presented, which are able to evaluate an interference pattern and reconstruct the two dimensional density profile of the gas-jet. Both programs start with an interference pattern as shown in figure 6.1.

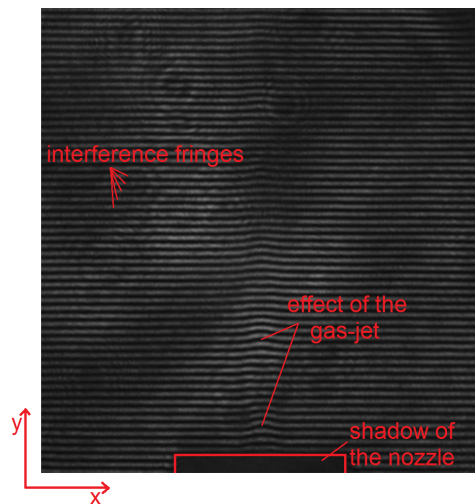


Figure 6.1 – Interference pattern of a nitrogen gas-jet expanding into room pressure (taken by Christina Westphälinger, edited). Parallel and almost horizontal interference fringes fill the pattern. The shadow of the nozzle is at the bottom of the image and the displacement effect of the gas-jet can be seen above it. The gas used is nitrogen expanding in y -direction at room temperature and into normal pressure with an inlet pressure of 8 bar.

6.1 F-interpolation program

The first program uses the F-interpolation to reconstruct the volume density of a gas-jet from an interference pattern. At first, the program loads the image with the interference pattern. Next, the program reads in a text document with information about the outlet width of the used nozzle, the laser wavelength and the gas type. These values are needed later and storing them in an external text document allows for a quick exchange of any of the values with no need to re-compile the whole program. Once all values are saved in variables, the size of the shadow of the nozzle in the interference pattern is measured. Therefore the brightness values of the image are filled in a two dimensional histogram using the ROOT package for C++. The average of the brightness of all pixels is calculated and an ordinate projection of the interference pattern with a width of one pixel is generated. The position of the projection is marked blue in figure 6.2 and the projection is shown in figure 6.3. The average brightness of all pixels is marked in figure 6.3 as a horizontal line at 22.79 a.u.. The projection shows a lower than average intensity at the position of the nozzle. The first pixel with a higher brightness in the projection marks the first interference fringe above the nozzle. In the shown example the 18th pixel is found as the first interference fringe. This value is used for the height of the nozzle. A coordinate projection of the interference pattern up to the height of the nozzle is generated and shown in figure 6.4. The projection area used is marked red in figure 6.2. The projection shows a lower brightness in the region of the nozzle compared with the regions on the left and right side of the nozzle. The width of the nozzle can be determined with a fit of two constant values A_i , one in the region of the nozzle A_2 and one in the outer region A_1 . The district of each value is estimated by additional fit variables B_i

$$f(x) = \begin{cases} A_1 & \text{for } x \leq B_1 \\ A_2 & \text{for } B_1 < x \leq B_2 \\ A_1 & \text{for } x > B_2 \end{cases} . \quad (6.1.1)$$

The difference of these variables is the width of the shadow of the nozzle $w_{\text{shadow}} = B_2 - B_1$. The ratio between the real width of the nozzle in μm and the width of the shadow of the

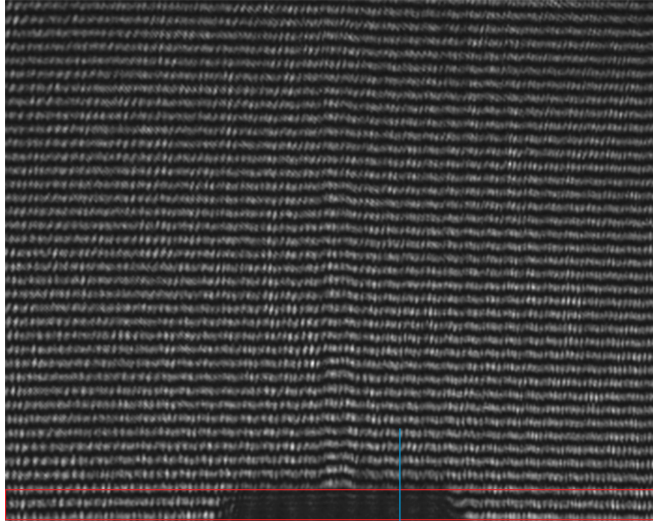


Figure 6.2 – Interference pattern of a gas-jet(taken by Christina Westphälinger, edited). The gas used is nitrogen expanding at room temperature into normal pressure with an inlet pressure of 8 bar. The blue line marks the ordinate projection area used for the determination of the height of the nozzle. The ordinate projection is shown in figure 6.3. The red area marks the coordinate projection area used for the determination of the width of the nozzle. The coordinate projection is shown in figure 6.4.

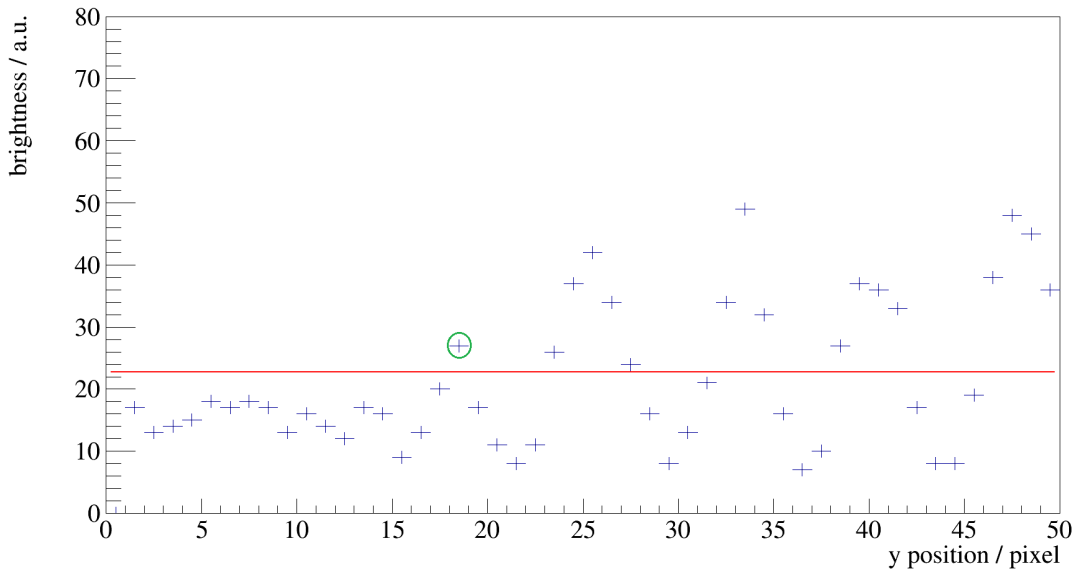


Figure 6.3 – Ordinate projection with a width of one pixel of the bottom region of the interference pattern. The red line marks the average brightness of the whole interference pattern. The first pixel with a higher than average brightness (the 18th pixel) is encircled in green and marks the first interference fringe.

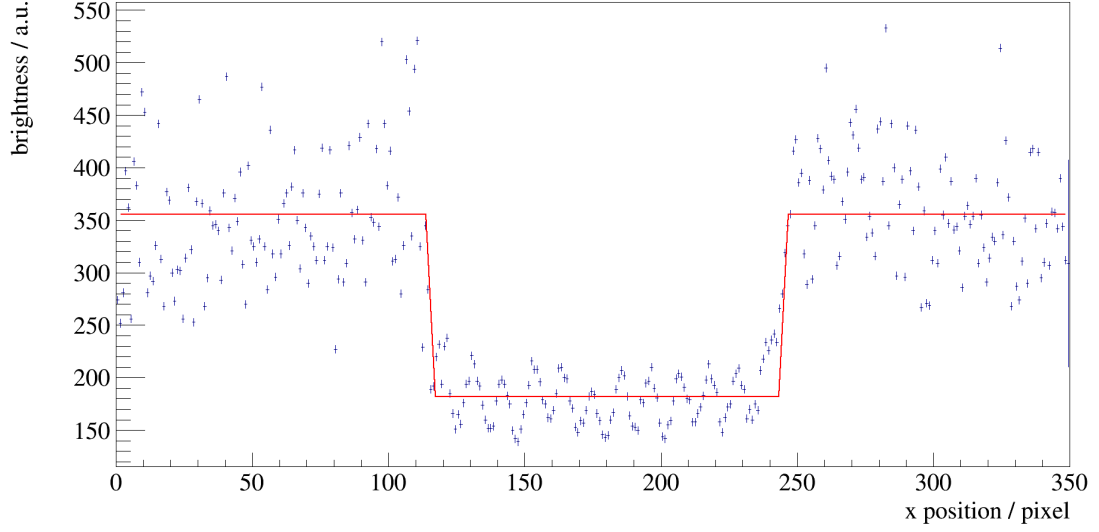


Figure 6.4 – Coordinate projection of the lower region of the interference pattern (cf. figure 6.2) with the fit of two constant values using formula 6.1.1 to estimate the width of the nozzle w_{shadow} .

nozzle in pixel is used for the conversion from the pixel scale to meters

$$c = \frac{w_{\text{real}}}{w_{\text{shadow}}} . \quad (6.1.2)$$

The program separates all interference fringes one by one. It searches on the most left side of the image for minima from bottom to top starting at the height of the first interference fringe. Every time a minimum is found the program starts to follow the progression of the minimum from left to right. In this way all interference fringes are separated. All found minima are drawn into the interference pattern and it is shown to the user, giving a first control stage. Figure 6.5 shows an interference pattern on the left side and the same interference pattern with the found minima marked at the right side. The program pauses at this point and waits for the user to push any key to continue.

The next part of the program evaluates one interference fringe at a time to reconstruct the gas-jet density for each height above the nozzle separately. The program takes a single interference fringe and reads its brightness values into a two dimensional histogram. An example for this is shown in figure 6.6. The zero valued bins belong to the next or

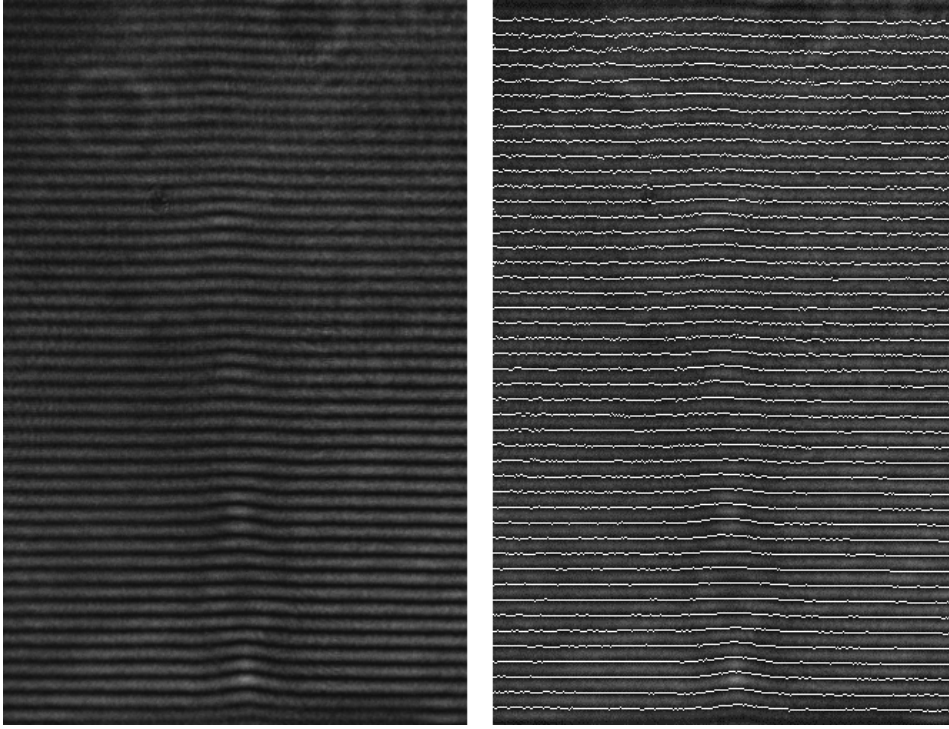


Figure 6.5 – On the left side is a photo of an interference pattern (taken by Christina Westphäliger). The gas used is nitrogen expanding at room temperature into normal pressure with an inlet pressure of 8 bar. The right side shows the same interference pattern, but the minima found by the first reconstruction program are marked.

the previous interference fringe. For each column of the interference fringe an ordinate projection is generated by the program. An example for this is shown in figure 6.7. A fit

$$g(x) = P_0 \sin^2 \left(\frac{x - P_1}{P_2} + \frac{\pi}{2} \right) + P_3 \quad (6.1.3)$$

with the fit parameters P_i is made at the projection. The phase parameter P_1 is limited to the values of the coordinate axis and defines the maximum position. This parameter is plotted against the column number. An example for this is shown in figure 6.8. In a first order approximation this graph shows the phases at a single height above the nozzle $\Delta\Phi_x$. A fit is made at the graph using formula 4.1.17 with an additional background

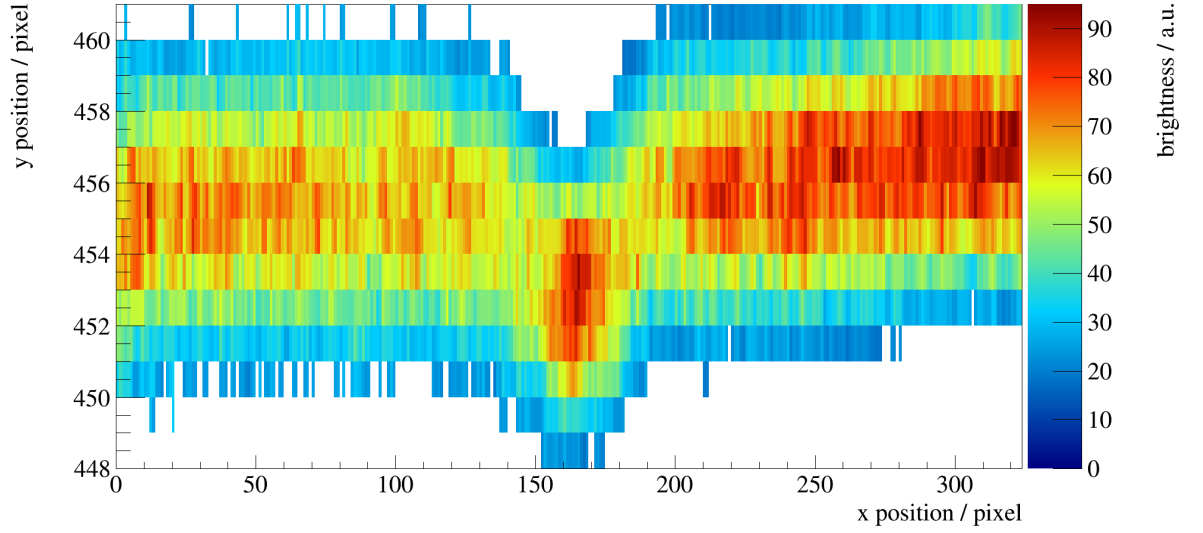


Figure 6.6 – The two dimensional histogram of a single interference fringe (from one brightness minimum to the next one). All bins without entries belong to other interference fringes. The 13th fringe above the nozzle is shown.

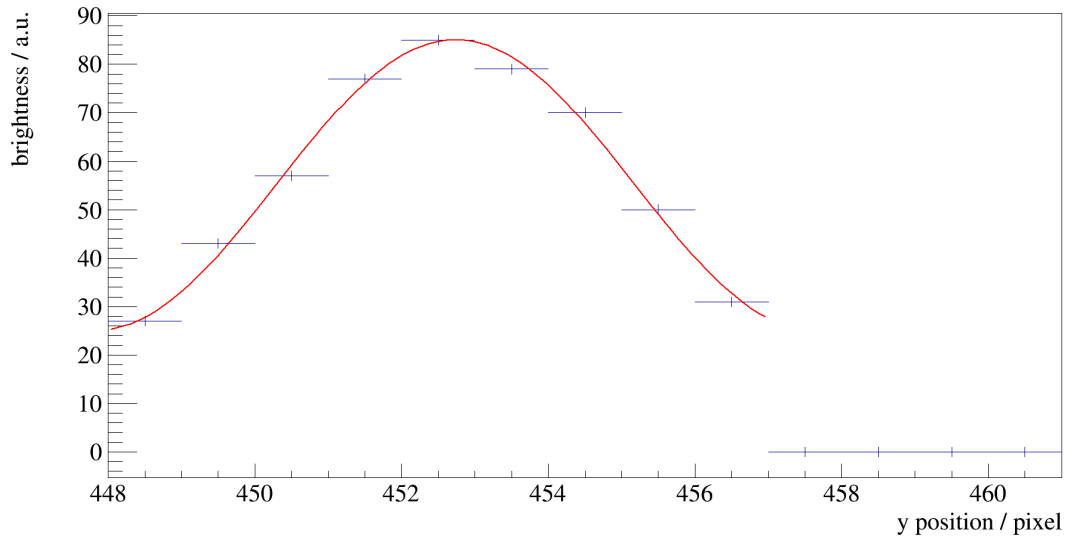


Figure 6.7 – The ordinate projection of a single column (column 161 is shown) and the corresponding sin fit using formula 6.1.3.

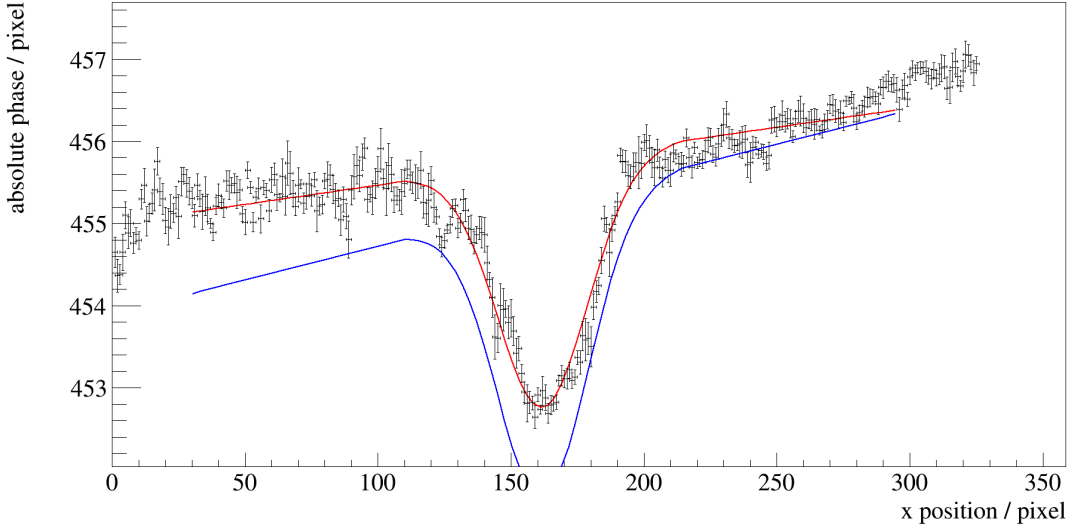


Figure 6.8 – Maximum positions of the individual sin fits at the ordinate projections of a single interference fringe. The fit of formula 6.1.4 is shown in red and the corresponding start parameters in blue.

$$\Delta\Phi_x(r) = A_x e^{-\frac{r^2}{B_x^2}} \operatorname{erf}\left(\frac{\sqrt{R_x^2 - y^2}}{B_x}\right) + C_x \cdot r + D_x \quad (6.1.4)$$

with the fit parameters A_x , B_x , C_x and D_x , the beam radius $R_x = 3\sigma = \frac{3B_x}{\sqrt{2}}$ and the linear offset $(C_x \cdot r + D_x)$, which has been chosen because the interference patterns are often sloped and the interference fringes not exactly horizontal. The parameter values of the previous fringe are used as start values for the next fringe. The parameters A_x and B_x are saved in a matrix and this procedure is repeated for each interference fringe. The volume density of the gas-jet can be reconstructed from the fit-parameters of each interference fringe using the assumption of the Gaussian shape for each height above the nozzle (cf. formula 4.1.15)

$$\rho_x(r) = a_x e^{-\frac{r^2}{b_x^2}}$$

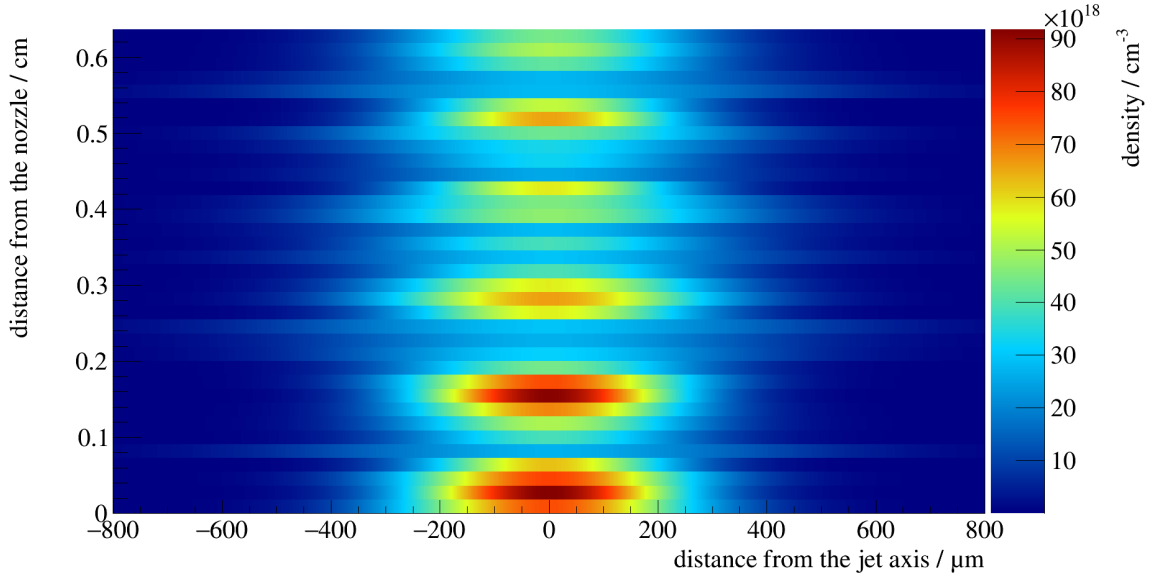


Figure 6.9 – A reconstructed density profile of a nitrogen gas-jet expanding at room temperature from $p_0 = 8$ bar into normal pressure. The used nozzle has a narrowest diameter of $d^* = 500 \mu\text{m}$. The corresponding interference pattern is shown in figure 6.5.

with the distance from the center of the gas beam r . For the conversion of the fit parameters A_x and B_x (cf. formula 6.1.4) to the density amplitude a_x and the density width b_x , formula 4.1.17 and formula 6.1.4 can be combined to

$$a_x = \frac{\lambda}{\pi^{3/2} k_{\text{GD}}} \cdot \frac{A_x}{B_x} \quad (6.1.5)$$

$$b_x = B_x \quad (6.1.6)$$

with the Gladstone-Dale constant k_{GD} already loaded from an external document and the laser wavelength λ . The example used nitrogen with a Gladstone-Dale constant of $k_{\text{GD, nitrogen}} = 1.11 \cdot 10^{-23} \text{ cm}^3$ and a HeNe-laser with a wavelength of $\lambda = 632.8 \text{ nm}$. The positions (in pixels) can be converted to distances (in m) using formula 6.1.2. Figure 6.9 shows the reconstructed density profile of the gas jet corresponding to the interference pattern shown in figure 6.5. The gas used is nitrogen and the jet expands from $p_0 = 8$ bar at room temperature into atmospheric pressure. Since the gas leaves the Laval nozzle with supersonic speed, the formation of shock diamonds is expected and can be observed

in the reconstructed density profile. Shock diamonds are standing waves generated by reflections of gas-jet at the surrounding air pressure [M⁺11]. The building of shock diamonds is a common phenomenon for jet engines and rockets flying in the atmosphere.

The F-interpolation program is able to reconstruct the density profiles of gas-jets from their corresponding interference patterns by F-interpolation. Although this works well, another program using the proportionality between phase shift and areal density of the gas-jet has been written to improve the spacial resolution in jet direction and to be more flexible with the shape of the gas-jet.

6.2 Fourier Transformation program

The second program uses the proportionality of phase shift and areal density (cf. formula 4.1.11) and calculates the phase shift from the interference pattern using fast forward Fourier Transformations in different image sections. The program reads in the interference pattern (a 8-bit greyscale image). As a second step the program loads the file 'InterferometerSettings.txt' from the same folder as the executive. This file contains information about the laser and the gas used, namely the values of the laser wavelength λ in nm, the atom mass m of the gas in the unified atomic mass unit u and the Gladstone-Dale constant k_{GD} of the gas in $\frac{\text{nm cm}^2}{\text{g}}$. This allows a swift change of setting to another gas with no need to re-compile the program. The information will be needed later for the conversion of phase-difference to area particle density.

After these preparations starts the analysis part of the program. The program calculates the two dimensional fast forward Fourier Transformation by formula 4.2.5 of a quadratic region around a pixel. The transformed region has a size of 32×32 pixels with the chosen pixel in the center of the region. Figure 6.10 shows an example for an interference pattern and a single transformation region. The magnitude and phase images are calculated by formula 4.2.2 and 4.2.3 and scaled to be greyscale 8-bit images. An example for the magnitude and the phase image is shown in figure 6.11. The relevant phase information for the chosen pixel is the phase of the carrier frequency, which is the frequency of the

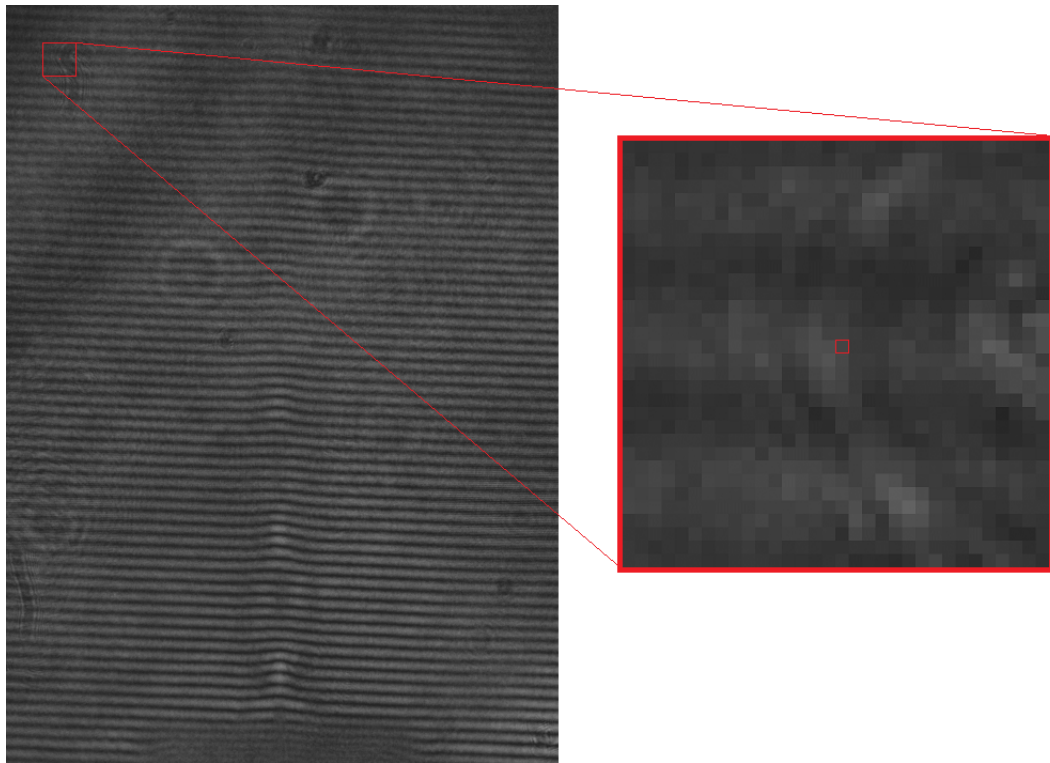


Figure 6.10 – On the left side is a photo of an interference pattern (taken by Christina Westphäliger). The gas used is nitrogen expanding at room temperature into normal pressure with an inlet pressure of 10 bar. On the right side is a single region for a Fourier Transformation with a size of 32×32 pixels. The central pixel is marked.

interference fringes without any effect of the gas-jet. The carrier frequency can be found in the magnitude spectrum showing the contributions of each frequency in x and in y direction. The carrier frequency is dominant in the y direction. The program searches for the carrier frequency as the maximum in the magnitude image on the y axis, while ignoring the origin. It is very important to select a size of the transformed region big enough to separate the carrier frequency from the origin. But very large transformed regions lead to smeared density profiles. A good compromise is a transformation region containing two to three interference fringes. The program now saves the phase from the phase image at the position of the carrier frequency as the phase of the pixel in the center of the transformed region. This procedure is repeated for each pixel except all pixels too close to the border of the image to be in the center of a transformation region. These pixels are not important for the evaluation and will be ignored.

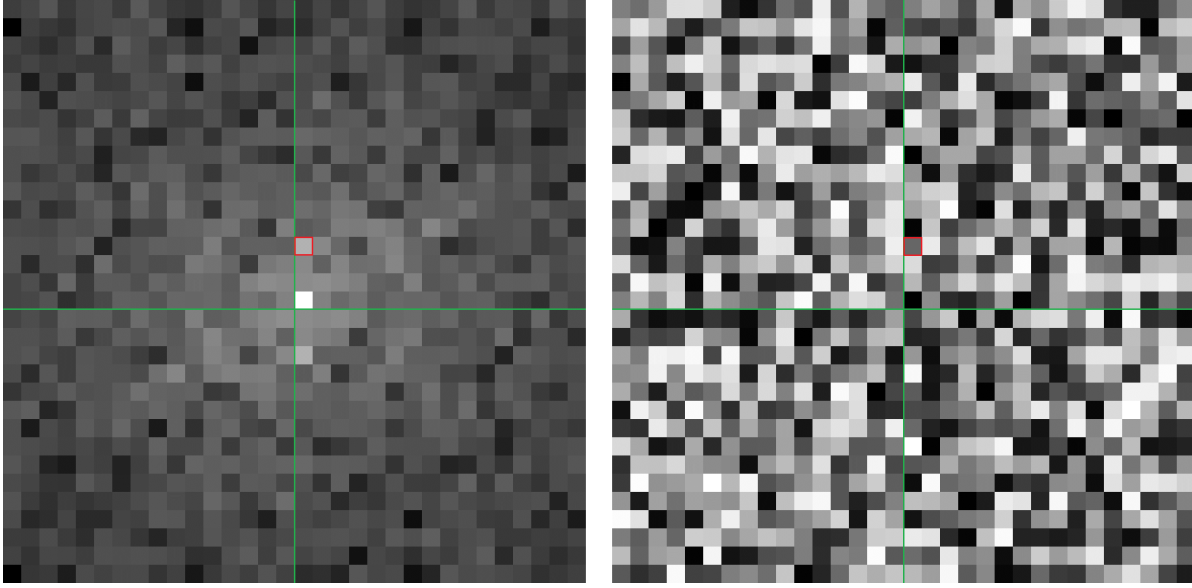


Figure 6.11 – Fourier Transformation of the Fourier Transformation region shown in figure 6.10: On the left side is the magnitude spectrum and on the right side is the phase spectrum. The carrier frequency is marked red, respectively. On the x Axis are the frequencies in x direction and on the y axis the frequencies in y direction. The origin is in the center of the images and marked green, respectively.

Up to now the phase of each important pixel has been evaluated. Every phase is between 0 and 2π , or for 8-bit values between 0 and 255. To get an explicit phase difference for each pixel the phases need to be transformed to be continuous. This is separately done for each row meaning for each height over the nozzle. An example for the calculated phases of one row is shown in figure 6.12. The transformation algorithm allows only phase-differences from one pixel to the next pixel of π or rather 123. Every phase that has a bigger difference to the phase of the pixel to its left is raised or lowered by 2π or rather 255. Without any gas-jet the continuous phases of one row should show a constant values or a linear slope if the interference fringes in the image are not exactly horizontal. Curved interference fringes are also possible resulting in slightly curved phase trends. The effect of the gas beam is a displacement of these phases. Figure 6.13 shows the smoothed phases with a second order polynomial fit using the first and the last 2/7 of the pixels for each row. The fit determines the reference phase for the row. The difference between this reference phase and the phase of a pixel is the phase-difference $\Delta\Phi$ of the pixel. These phase-differences are calculated for each pixel using the reference phases from the fits for each row.

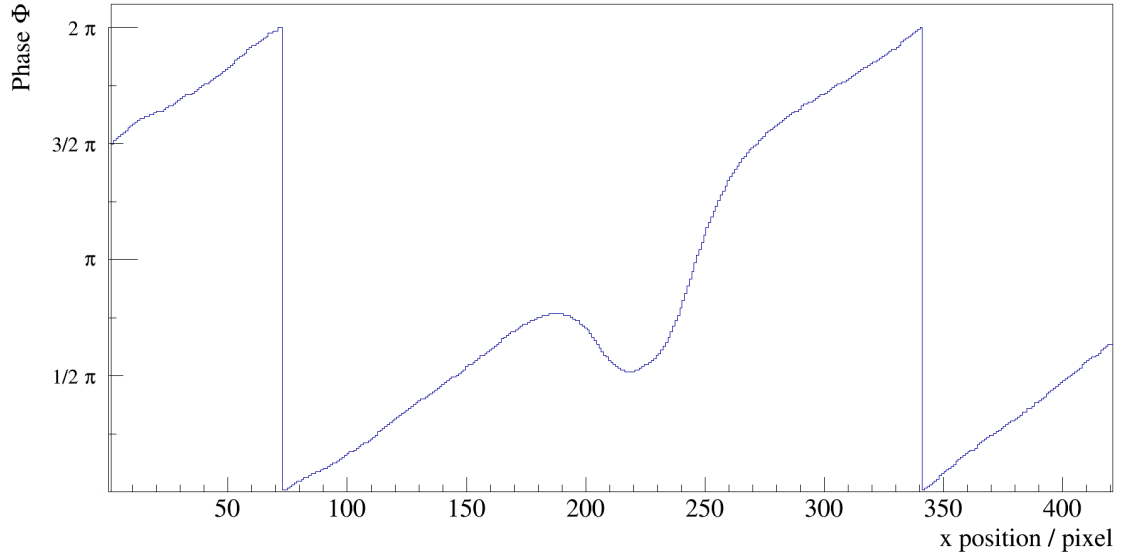


Figure 6.12 – Phases of the carrier frequency for one row of the image as they are calculated by the Fourier Transformation. The phase shift caused by the gas-jet can be seen around pixel 220.

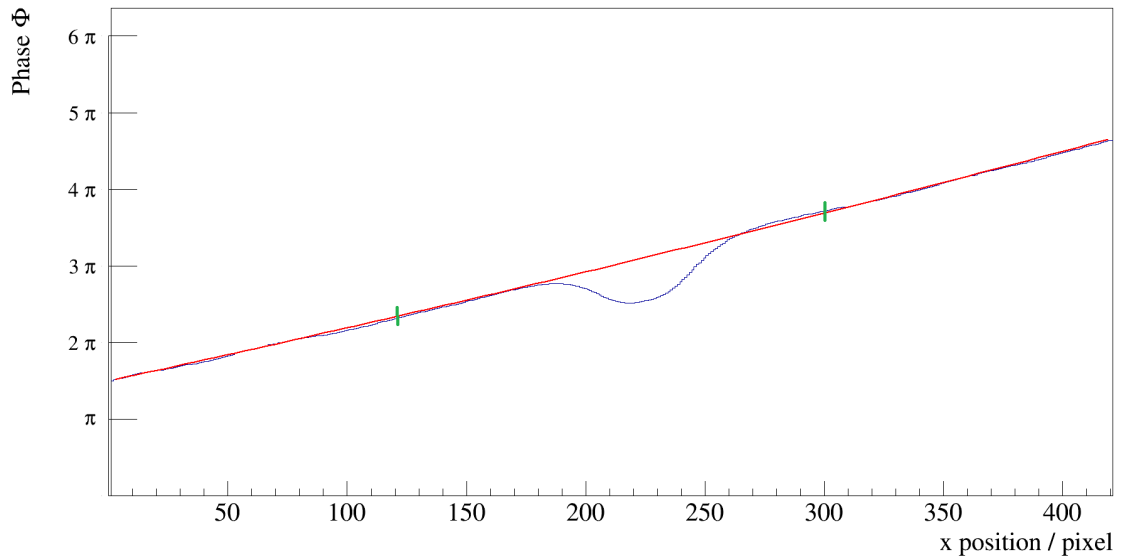


Figure 6.13 – Continuous phases of the carrier frequency for one row of the image with a second grade polynomial reference fit using the outer 4/7 of the continuous phases. The green marks are showing the fit range.

The calculated phase-differences are converted to areal particle densities by equation 4.1.11

$$\rho_A(x, y) = \frac{\Delta\Phi(x, y)}{2\pi} \frac{\lambda}{k_{GD}} .$$

The wavelength of the used laser λ and the Gladstone-Dale constant k_{GD} have been loaded from the settings file at the very beginning of the main program. The result is filled into a two dimensional histogram and printed as a '.png' image and for further editing as a '.root' file. In figure 6.14 is an example for the output.

The reconstructed areal density profile shows six shock diamonds, while the intensity decreases for higher distances from the nozzle. Similar to the reconstructed density profile in figure 6.9, the building of shock diamonds is expected. For a more precise determination of the reconstructed areal density profile shown in figure 6.14, an ordinate projection of the center of the reconstructed gas-jet is shown in figure 6.15. The six shock diamonds and the decreasing intensity can be observed clearly.

The uncertainty of the reconstructed areal density profiles depends on the taken interference pattern, on the size of the chosen Fourier Transformation area and on the uncertainties of the reference fits. The different interference patterns taken vary in their local brightness and the distance between the single interference fringes can be adjusted with the Mach-Zehnder interferometer. The uncertainties caused by these two factors can not be determined with the test setup as it was used for this work. The uncertainty caused by the size of the Fourier Transformation area has been examined qualitatively: Bigger transformation regions smear out the reconstructed areal density profile and result in lower areal densities, while smaller transformation areas result in slightly higher densities of up to $\rho_A = 4.7 \cdot 10^{18} \text{ cm}^{-2}$ compared with the reconstructed areal density of the used transformation region $\rho_A = 4.4 \cdot 10^{18} \text{ cm}^{-2}$. The uncertainties caused by the reference fits resulted in an uncertainty for the reconstructed maximal areal density of 5% – 10%.

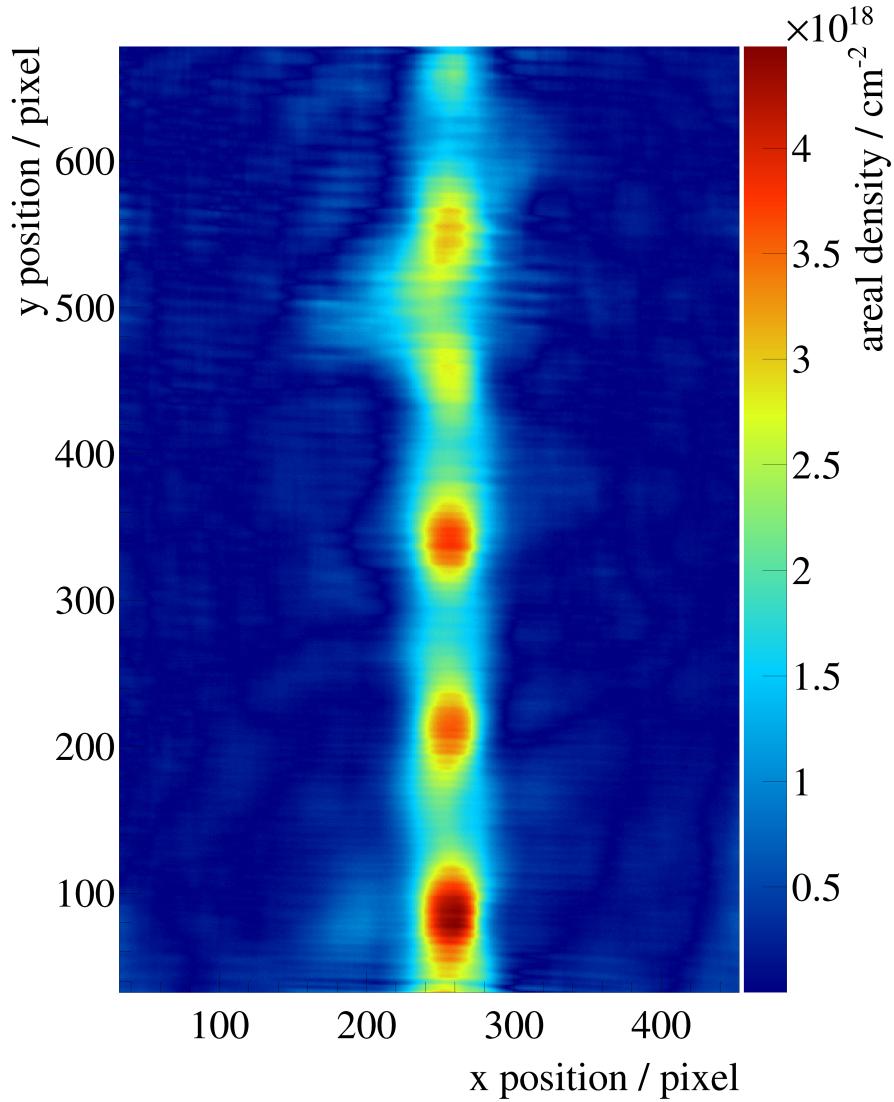


Figure 6.14 – A reconstructed density profile of a nitrogen gas-jet expanding at room temperature from $p_0 = 10$ bar into normal pressure. The nozzle used has a narrowest diameter of $d^* = 500 \mu\text{m}$. The corresponding interference pattern is shown in figure 6.10. 100 pixels correspond to 1.36 mm.

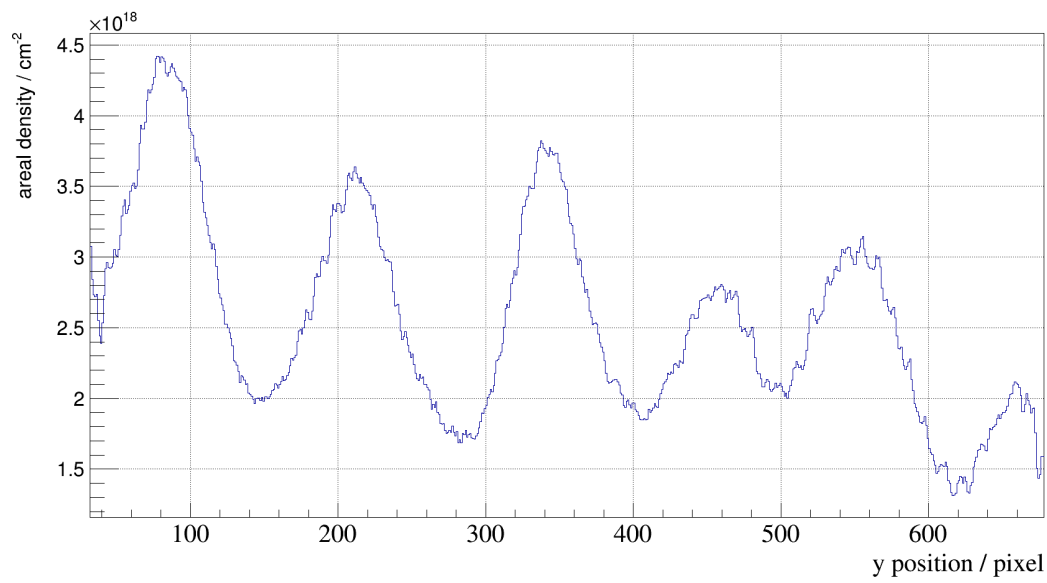


Figure 6.15 – Ordinate projection of the center of the reconstructed areal density profile shown in figure 6.14. The areal density decreases with the distance from the nozzle and six shock diamonds can be seen. 100 pixels correspond to 1.36 mm.

7 Measurements on the gas target for MAGIX

Since MAGIX requires a high target areal density of $\rho_A = 10^{19} \text{ cm}^{-2}$ directly behind the nozzle of the target, measurements on the density profile of the MCT-M have been done and will be presented in this chapter. These measurements also contain information about the shape of the gas-jet, which can be used to determine the distance and the shape of the catcher for MAGIX. Next to the measurements on nitrogen jets with different pressures before the nozzle p_0 , this chapter contains theoretical calculations for a comparison with the measured data.

7.1 Comparison with theoretical calculations

Theoretical calculations have been done for a comparison with the reconstructed areal densities, based on the detailed derivation by Alexander Täschner [Täs12]. For these calculations the gas has been assumed to be a perfect gas, meaning the ideal gas law

$$pV = nRT \tag{7.1.1}$$

$$\text{and } c_p - c_V = nR \tag{7.1.2}$$

with the pressure p , the volume V , the amount of substance n and the gas constant $R = 8.314456(10) \frac{\text{J}}{\text{Kmol}}$ [MTN12] is valid and the heat capacities c_p and c_V are assumed constant. The mass flow \dot{m} of a gas through a sectional area A with a velocity v is

$$\dot{m} = \rho v A . \quad (7.1.3)$$

The outlet area of the nozzle can be used as the sectional area A and the velocity v can be calculated using energy conservation

$$h_0 + \frac{v_0^2}{2} = h + \frac{v^2}{2} \quad (7.1.4)$$

with the reference enthalpy h_0 , the current enthalpy h and the reference velocities v_0 . Assuming the reference point in front of the nozzle where the gas is at rest $v_0 = 0$ leads to

$$v = \sqrt{2(h_0 - h)} . \quad (7.1.5)$$

The enthalpy h can be substituted by using the perfect gas properties

$$c_p = \frac{\kappa}{\kappa - 1} \frac{R}{M} \quad (7.1.6)$$

$$\text{and } h = c_p T \quad (7.1.7)$$

$$= \frac{\kappa}{\kappa - 1} \frac{R}{M} T \quad (7.1.8)$$

with the molar mass M and the heat capacity ratio $\kappa = \frac{Z+2}{Z}$ with the number of degrees of freedoms Z . A perfect gas has only three translation degrees of freedoms resulting in $\kappa = \frac{5}{3}$. This leads to

$$v = \sqrt{2c_p(T_0 - T)} \quad (7.1.9)$$

$$= \sqrt{\frac{2\kappa}{\kappa - 1} \frac{RT_0}{M}} \quad (7.1.10)$$

with the temperature in front of the nozzle T_0 and the approximation $T = 0$. Neglecting the gas temperature behind the nozzle is a good approximation, because the temperature of a gas passing a Laval nozzle drops by adiabatic cooling (cf. chapter 3.2). The mass flow from formula 7.1.3 can be rewritten using formula 7.1.10 as

$$\dot{m} = \rho A \sqrt{\frac{2\kappa}{\kappa - 1} \frac{RT_0}{M}}. \quad (7.1.11)$$

The mass flow can also be calculated at the narrowest sectional area of the nozzle. All quantities at the narrowest sectional area are marked with a *. Formula 7.1.3 turns into

$$\dot{m}^* = A^* \rho^* v^* \quad (7.1.12)$$

$$= A^* \underbrace{\rho_0 \left(\frac{2}{\kappa + 1} \right)^{\frac{1}{\kappa - 1}}}_{\rho^*} \underbrace{\sqrt{\frac{2\kappa}{\kappa + 1} \frac{RT_0}{M}}}_{v^*} \quad (7.1.13)$$

using the density at the narrowest sectional area $\rho^* = \rho_0 \left(\frac{2}{\kappa + 1} \right)^{\frac{1}{\kappa - 1}}$ and the velocity at the narrowest sectional area $v^* = \sqrt{\frac{2\kappa}{\kappa + 1} \frac{RT_0}{M}}$, which can be calculated from the adiabatic flow of a perfect gas. This results in $\rho_0 = p_0 \frac{M}{RT_0}$ with the pressure in front of the nozzle p_0 , too. The mass flow at the narrowest sectional area can be rewritten as

$$\dot{m}^* = \frac{M}{R} A^* \frac{p_0}{\sqrt{MT_0}} \sqrt{\kappa R} \left(\frac{2}{\kappa + 1} \right)^{\frac{\kappa + 1}{2(\kappa - 1)}}. \quad (7.1.14)$$

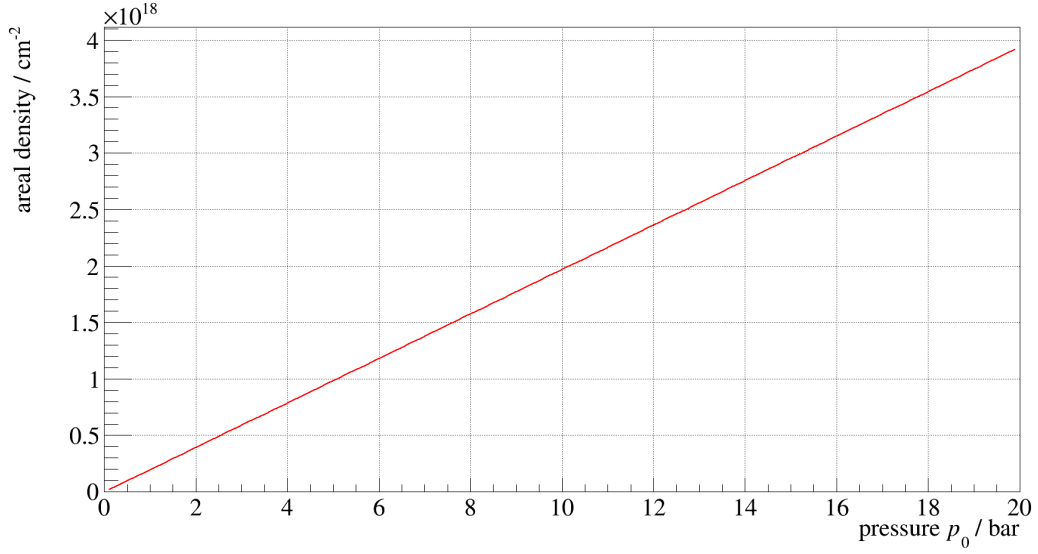


Figure 7.1 – Calculated densities for a nitrogen gas jet using formula 7.1.15 at the outlet of a Laval nozzle with an outlet diameter of $d = 2000 \mu\text{m}$ and a narrowest diameter of $d^* = 350 \mu\text{m}$ at room temperature. The plotted pressure p_0 is in front of the nozzle.

The assumption that there is no matter lost in the gas jet from the narrowest sectional area up to the nozzle outlet allows to equalise the mass flows \dot{m} and \dot{m}^* . The equations 7.1.11 and 7.1.14 can be combined to find

$$\rho = \frac{MA^*p_0}{RAT_0} \sqrt{\frac{\kappa-1}{2}} \left(\frac{2}{\kappa+1} \right)^{\frac{\kappa+1}{2(\kappa-1)}}. \quad (7.1.15)$$

Figure 7.1 shows a plot of the theoretically calculated densities of a nitrogen gas jet at the outlet of the nozzle with a diameter of $d = 2000 \mu\text{m}$ after passing a Laval nozzle with a narrowest diameter of $d^* = 350 \mu\text{m}$ for different pressures in front of the nozzle and at room temperature.

The areal density can be calculated by using the volume flow, too. The volume flow of the gas jet is defined as

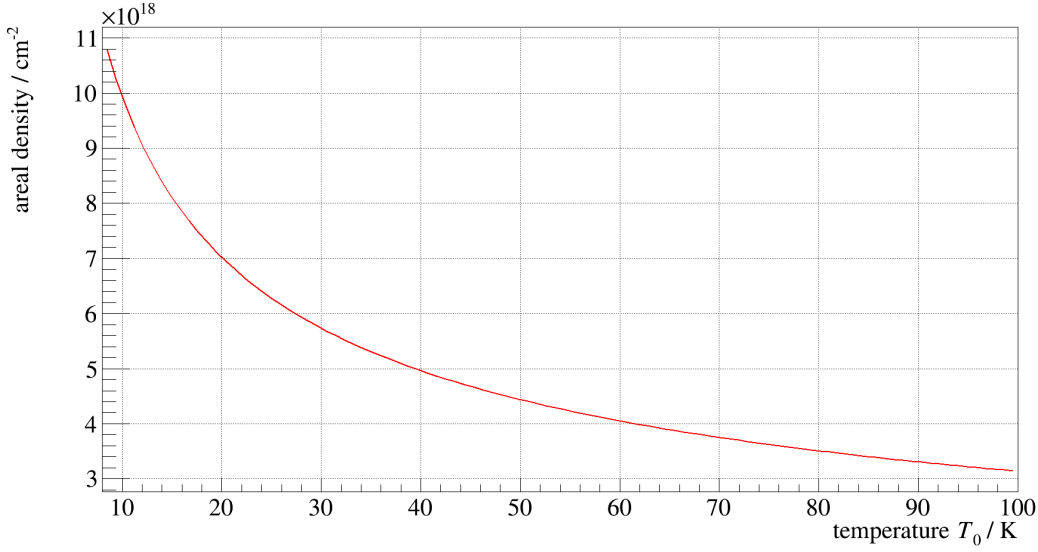


Figure 7.2 – Calculated density of a hydrogen gas jet at the outlet ($d = 1000 \mu\text{m}$) of a Laval nozzle with a narrowest diameter $d^* = 500 \mu\text{m}$ as a function of the gas temperature in front of the nozzle T_0 . The density has been calculated by formula 7.1.17 using a gas flow of $q_V = 40 \frac{\ell_n}{\text{min}}$.

$$q_V = \dot{m} \frac{R}{M} \frac{T_N}{p_N} \quad (7.1.16)$$

with the pressure and the temperature at normal conditions $p_N = 1.01325 \text{ bar}$ and $T_N = 273.15 \text{ K}$ and leads together with formula 7.1.11 to

$$\rho = \frac{q_V}{A} \frac{p_N}{T_N} \sqrt{\frac{\kappa - 1}{2\kappa}} \frac{M^3}{R^3} \frac{1}{\sqrt{T_0}}. \quad (7.1.17)$$

The theoretical expected density for a nitrogen gas-jet at room temperature with a volume flow of $40 \frac{\ell_n}{\text{min}}$ at the outlet of a nozzle with an outlet diameter of $d = 2000 \mu\text{m}$ using formula 7.1.17 is $\rho_{A, \text{theo}} = 2.43 \cdot 10^{18} \text{ cm}^{-2}$.

The estimated volume flow of MAGIX $q_V = 40 \frac{\ell_n}{\text{min}}$ results for a hydrogen gas-jet passing a nozzle with an outlet diameter of $d = 1000 \mu\text{m}$ and a narrowest diameter of $d^* = 500 \mu\text{m}$

at the lowest possible temperature provided by the used coldhead (cf. chapter 5) for the estimated gas flow $T_0 = 40\text{ K}$ [Gri17] according to formula 7.1.17 in $\rho_A = 5 \cdot 10^{18} \frac{\text{atoms}}{\text{cm}^2}$. Figure 7.2 shows a plot of formula 7.1.17 for this gas-jet. A nozzle with a rectangular outlet section could increase the reached areal density by a factor two resulting in the design density of MAGIX $\rho_{A, \text{ design}} = 10^{19} \frac{\text{atoms}}{\text{cm}^2}$.

7.2 Nitrogen jets

After the successful adjustment of the Mach-Zehnder interferometer on its new frame, measurements of the density and the beam profile have been done. Several images of interference patterns of nitrogen gas-jets at room temperature and at $p_0 = 9.5\text{ bar} - 20\text{ bar}$ in front of the nozzle have been taken in steps of 0.5 bar . The gas pressure has been pre-adjusted with a pressure reducing regulator and the precise values have been adjusted with a valve in combination with a baratron. The experimental setup of the gas target and the Mach-Zehnder interferometer used is described in chapter 5. The Laval nozzle used has a narrowest diameter of $d^* = 350\text{ }\mu\text{m}$ and an outlet diameter of $d = 2000\text{ }\mu\text{m}$. The best possible vacuum has been applied to the interaction chamber, resulting in a pressure of $p = 0.7\text{ mbar} - 1.66\text{ mbar}$ depending on the gas pressure. All interference patterns taken are analysed with the Fourier Transformation program presented in chapter 6.2. A Canon EOS 1100D has been used.

Figure 7.3 shows the interesting region of an image of an interference pattern. The shadow of the nozzle can be seen at the bottom of the image. A slight displacement effect in the interference fringes above the shadow of the nozzle can be seen, too. Figure 7.4 shows the corresponding reconstructed areal density profile as an example for the whole series of measurements, while all other reconstructed areal density profiles at different pressures in front of the nozzle can be found in the appendix A.1. The nozzle can be seen at the bottom of the image and a gas-jet slightly above the nozzle. Some background of $\approx 1 \cdot 10^{18} \text{ cm}^{-2}$ can be observed across the whole reconstructed image. The divergent gas-jet reaches a width of approximately 1.5 mm at a height of approximately 4 mm over the nozzle. Up to this height, the maximal areal density and the width of the gas-jet

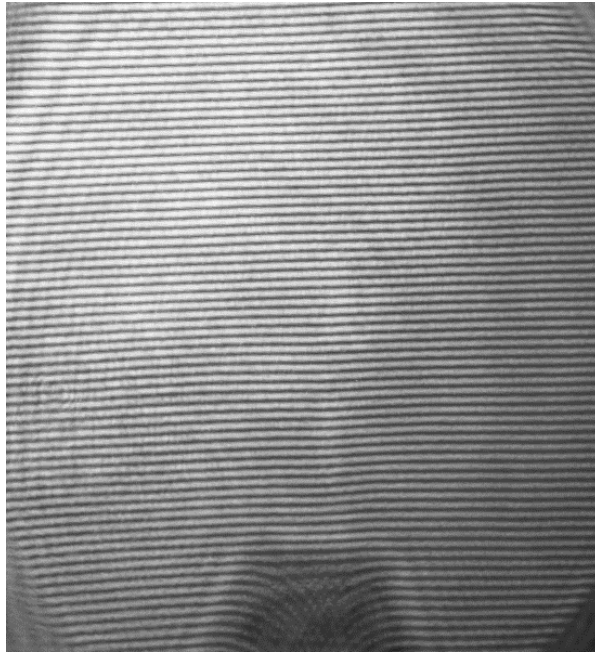


Figure 7.3 – Interference pattern of a nitrogen gas-jet at room temperature with a primary pressure of $p_0 = 18.5$ bar expanding into a vacuum of $p = 1.53$ mbar.

grows. The shape of the gas-jet is a slightly divergent cone, but shows the highest density at a height of ≈ 2 mm above the nozzle like a shock diamond. This is a result of the high pressure in the interaction chamber. Table A.1 in the appendix lists the maximal areal densities from the reconstructed areal density profiles and the corresponding pressure in the interaction chamber. The maximal areal density has been evaluated by taking the highest bin value in the reconstructed areal density profile ignoring the area of the nozzle and the corners. Figure 7.5 shows the maximal areal densities of all measured nitrogen jets plotted against the pressure in front of the nozzle. The theoretical prediction derived in the last section has been added to the figure. The data show an approximately linear behaviour. The values for higher inlet pressures are slightly below the theoretical prediction. The origin of these slightly lower values could be the high pressure in the interaction chamber at high inlet pressures or the assumption made for the theoretical calculation (e.g. perfect gas properties). The good agreement of theory and experiment shows that the experimental setup and the written reconstruction program work well.

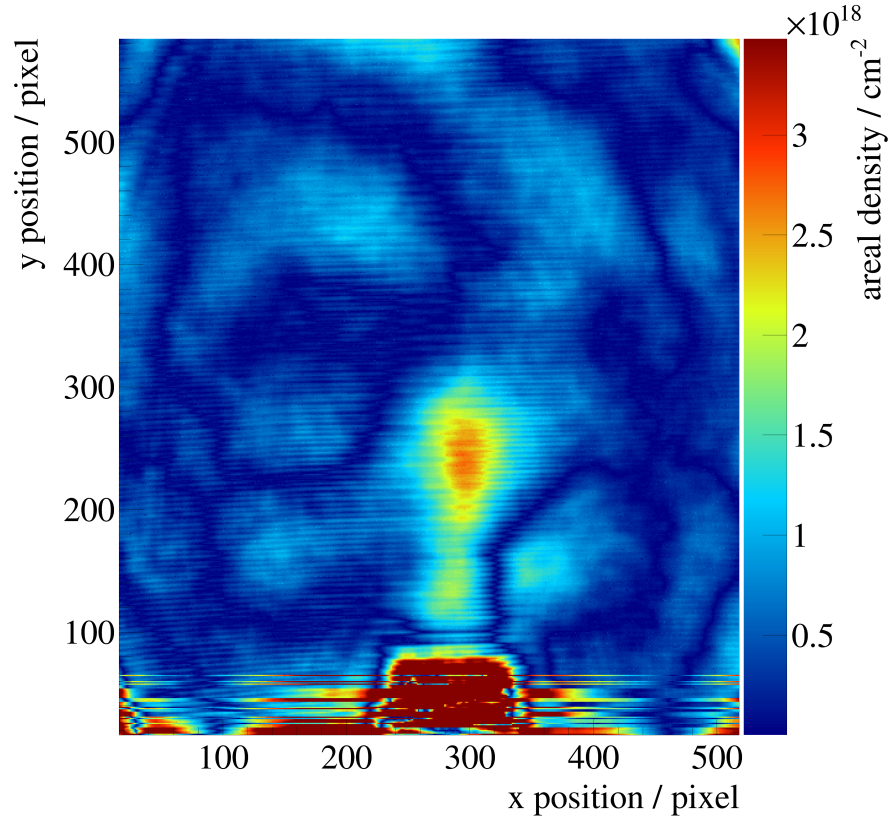


Figure 7.4 – Reconstructed density profile of a nitrogen gas-jet at room temperature with a primary pressure of $p_0 = 18.5$ bar expanding into a vacuum of $p = 1.53$ mbar. 100 pixels correspond to 1.18 mm.

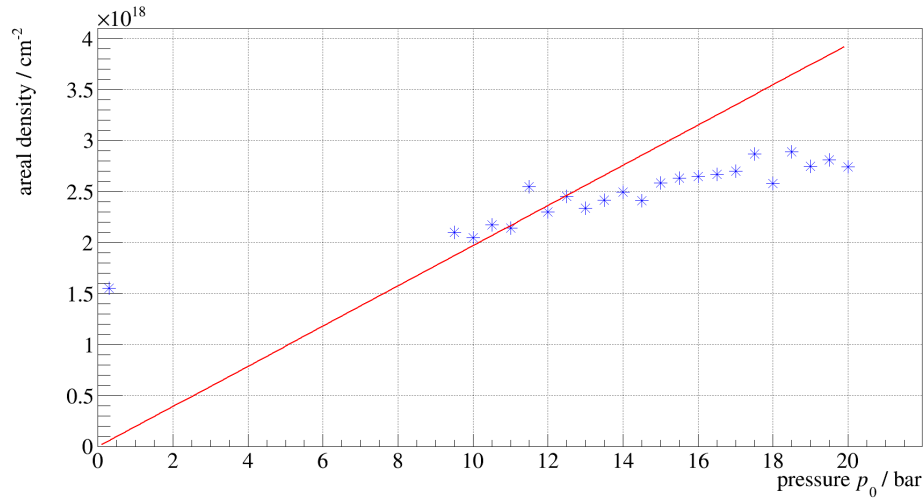


Figure 7.5 – Maximal areal densities of nitrogen gas-jets ρ_A expanding into a vacuum of $p = 0.7$ mbar – 1.66 mbar plotted against the pressure in front of the nozzle p_0 . The red line represents the theoretical calculated values using formula 7.1.15.

8 Summary and Outlook

The gas-jet target for MAGIX (MCT-M) has been launched in a test setup at the department of nuclear physics of the Westfälische Wilhelms-Universität Münster. A Mach-Zehnder interferometer has been built around the MCT-M on a decoupled aluminium frame, reproducing the interference effects observed by Christina Westphälinger (s. [Wes16]). The test beam of the interferometer enters the interaction chamber through an acrylic glass flange, passes the gas-jet and leaves the interaction chamber through another acrylic glass flange. Interference patterns with a high contrast and clearly visible interference fringes have been observed. The Mach-Zehnder interferometer has been optimised with a spatial filter to improve the laser profile. The test setup enables a monitoring of the gas target without any influence on it and therefore is a control stage for the stability and the density of the target.

Two programs have been written to determine the density profile of the gas-jet from the corresponding interference pattern. One program uses the F-interpolation and assumes a Gaussian shape for the gas-jet particle density. The other program uses Fourier Transformation to determine the phase difference of each pixel in the interference pattern, which is proportional to the areal particle density. Both programs work well and result in two dimensional (areal) density profiles of the examined gas-jet.

Basic measurements on the gas-jet density profile of the MCT-M have been done. The Laval nozzle used had a narrowest diameter of $d^* = 350 \mu\text{m}$ and an outlet diameter of $d = 2000 \mu\text{m}$. The expected density shapes have been observed: Gas-jets expanding into room pressure showed the formation of shock diamonds and gas-jets expanding into a vacuum showed a more divergent shape without shock diamonds. A series of measurements with inlet pressures from 9.5 bar to 20 bar resulted in a maximal areal density $\rho_A = 2.888 \cdot 10^{18} \text{ cm}^{-2}$ at an inlet pressure of $p_0 = 18.5 \text{ bar}$ for nitrogen gas-jets at room temperature. A very stable background of $\approx 1 \cdot 10^{18} \text{ cm}^{-2}$ has been observed. The reconstructed areal densities fit roughly with the theoretical calculated prediction,

showing that the constructed test setup of gas-jet target and Mach-Zehnder interferometer works well. This allows for a determination of the luminosity for a fixed target experiment.

The test setup will be used for several measurements on gas-jet areal density profiles. There will be tests with different nozzles, different gases and at lower temperatures by S. Grieser [Gri17]. Systematic measurements can be done to determine the final nozzle for MAGIX, the distance and the shape of the catcher for MAGIX, and the final luminosity. A new nozzle design has been developed by D. Bonaventura, A. Khoukaz and S. Grieser and is shown in figure 8.1. The new design features a smaller nozzle and a separate connection to the coldhead. This reduces the production costs and effort for new nozzles, since the separate connection can be used for all nozzles. The copper connection has a better thermal conductivity compared to the stainless steel used beforehand resulting in a lower possible temperature at the outlet of the nozzle. If the design density of MAGIX can not be reached with the gas-jet target, nozzles with a rectangular outlet area may be used to increase the areal density of the target. In addition to that, measurements on the development over time of gas-jet can be done using a camera without shutter able to take pictures of the interference pattern in quick success. This may help running the target later at MESA by investigating a possible pulsed operation mode of the target to reduce the background pressure in the interaction chamber.

Further improvements of the reconstruction programs are possible and especially the uncertainties have to be better evaluated.

The MCT-M will be installed at MAMI for first test in summer 2017 and move on to MESA as soon as it is built. The further development of the gas-jet target for MAGIX can be found in [Gri17].

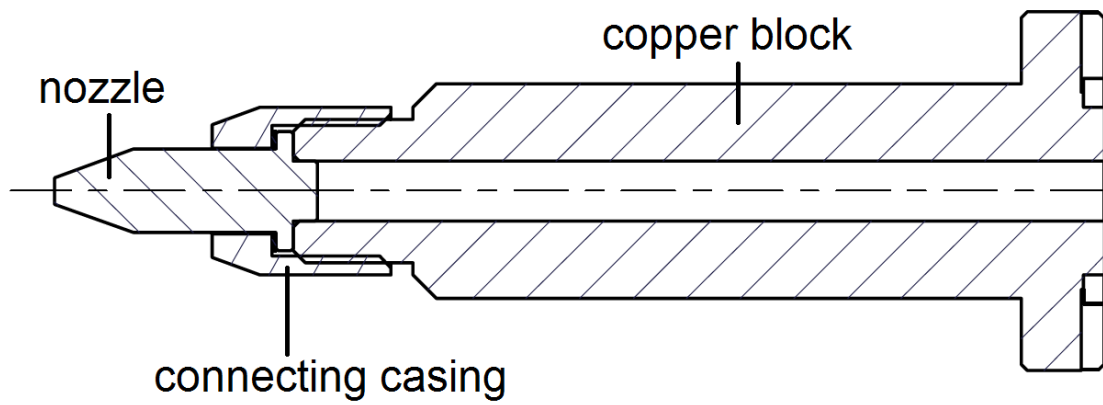


Figure 8.1 – The new nozzle design, here without inner geometry (generated by Daniel Bonaventura, edited). The new nozzle is very small and mounted on a copper block.

A Appendix

A.1 Reconstructed areal density profiles

The images A.1 to A.23 are showing the reconstructed areal density profiles from the measurements presented in chapter 7.

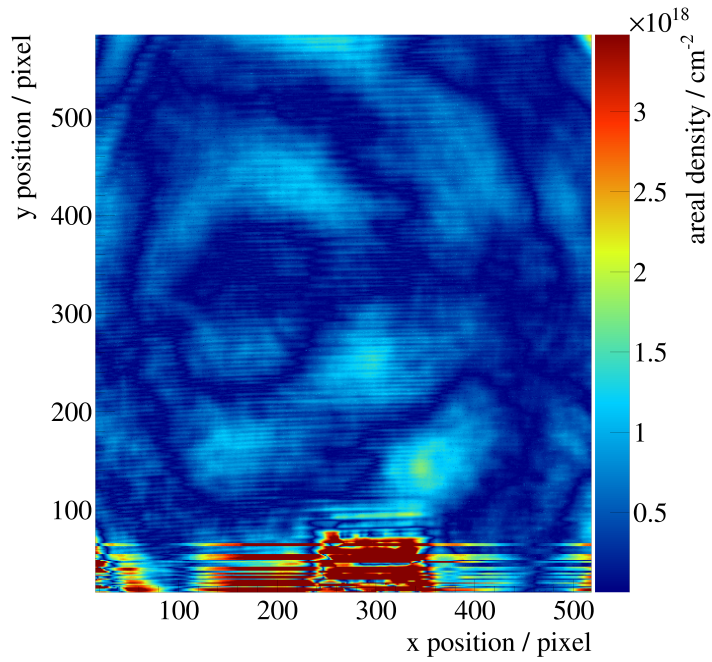


Figure A.1 – Reconstructed density profile of a nitrogen gas-jet at room temperature with a primary pressure of $p_0 = 0.3$ bar expanding into a vacuum of $p = 0.008$ mbar. 100 pixels correspond to 1.18 mm.

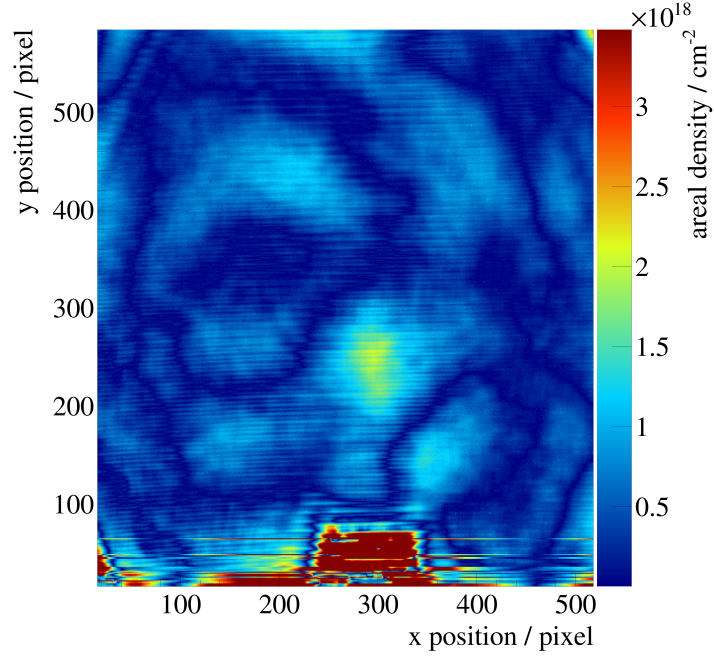


Figure A.2 – Reconstructed density profile of a nitrogen gas-jet at room temperature with a primary pressure of $p_0 = 9.5$ bar expanding into a vacuum of $p = 0.7$ mbar. 100 pixels correspond to 1.18 mm.

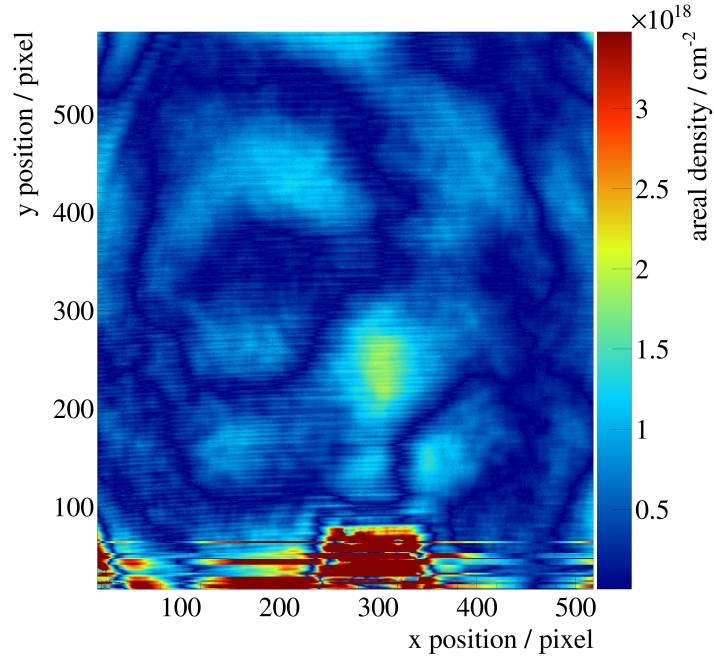


Figure A.3 – Reconstructed density profile of a nitrogen gas-jet at room temperature with a primary pressure of $p_0 = 10$ bar expanding into a vacuum of $p = 0.81$ mbar. 100 pixels correspond to 1.18 mm.

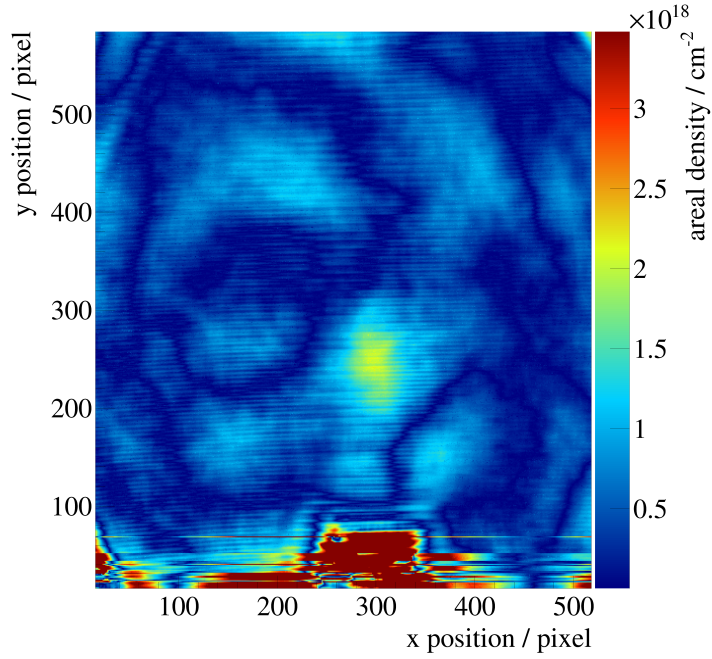


Figure A.4 – Reconstructed density profile of a nitrogen gas-jet at room temperature with a primary pressure of $p_0 = 10.5$ bar expanding into a vacuum of $p = 0.84$ mbar. 100 pixels correspond to 1.18 mm.

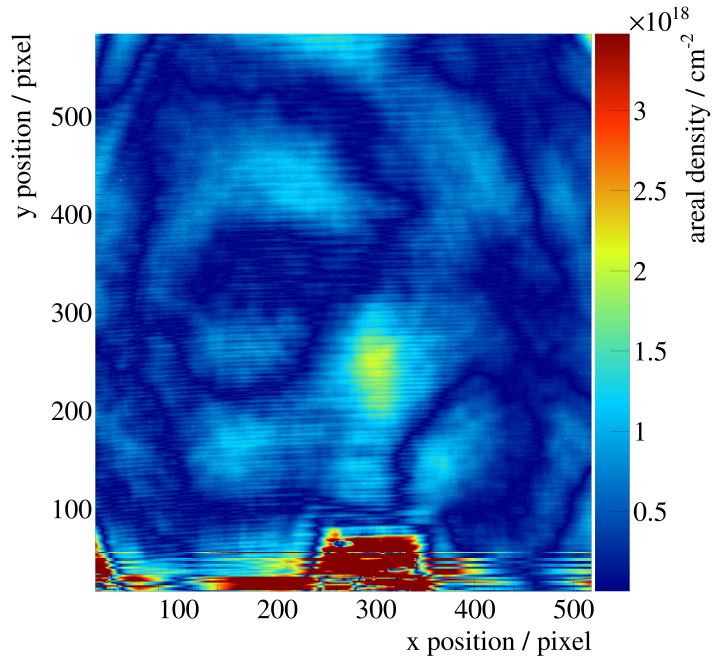


Figure A.5 – Reconstructed density profile of a nitrogen gas-jet at room temperature with a primary pressure of $p_0 = 11$ bar expanding into a vacuum of $p = 0.89$ mbar. 100 pixels correspond to 1.18 mm.

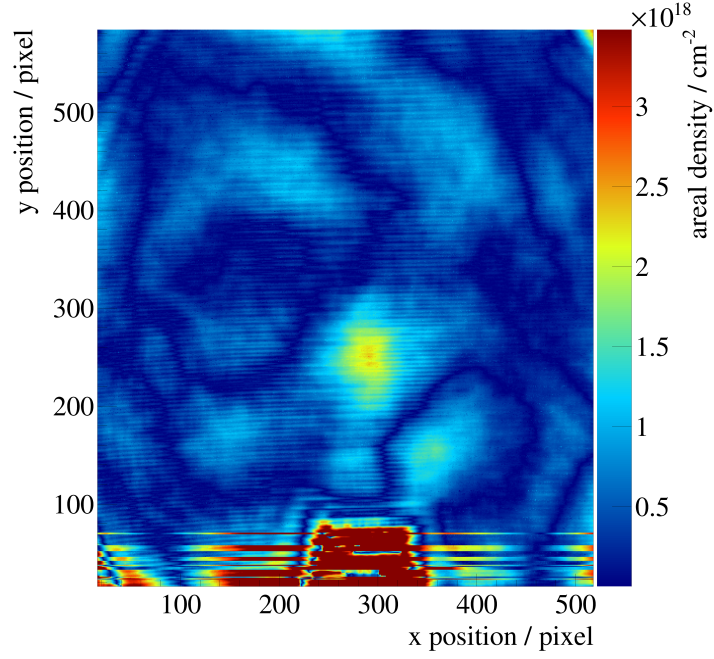


Figure A.6 – Reconstructed density profile of a nitrogen gas-jet at room temperature with a primary pressure of $p_0 = 11.5$ bar expanding into a vacuum of $p = 0.94$ mbar. 100 pixels correspond to 1.18 mm.

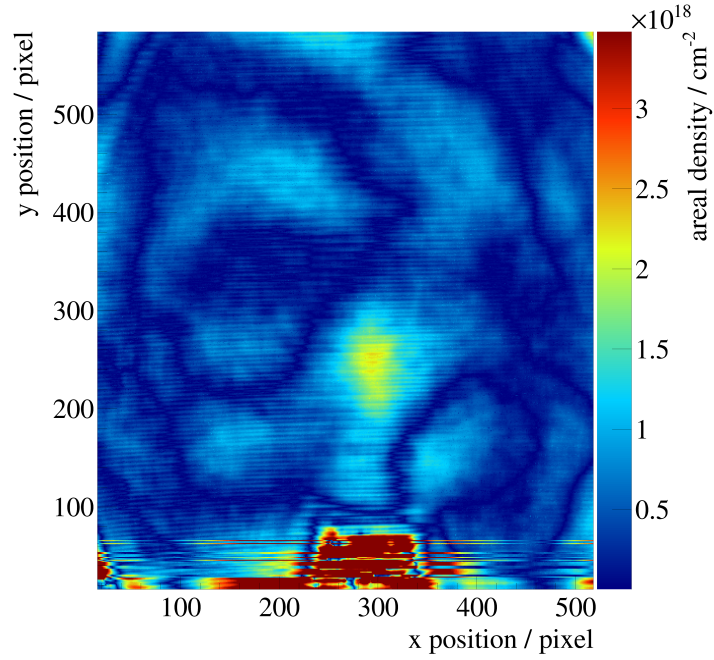


Figure A.7 – Reconstructed density profile of a nitrogen gas-jet at room temperature with a primary pressure of $p_0 = 12$ bar expanding into a vacuum of $p = 0.98$ mbar. 100 pixels correspond to 1.18 mm.

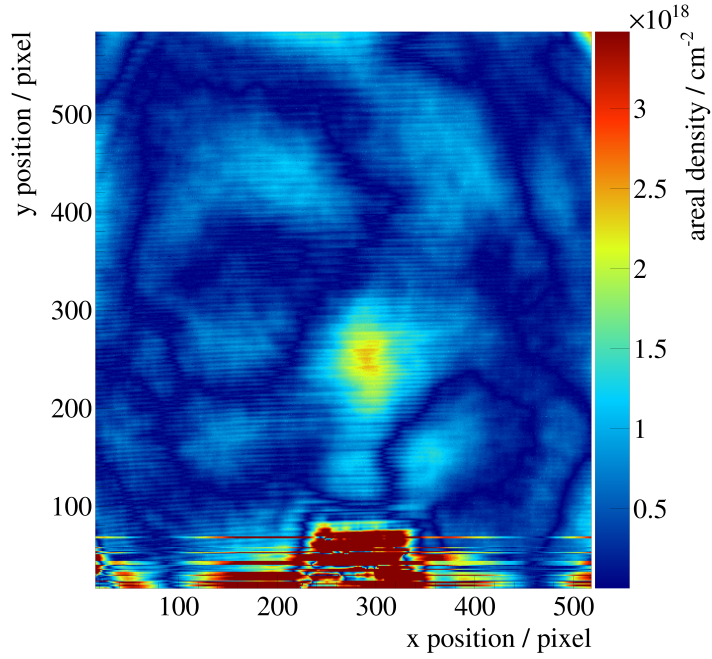


Figure A.8 – Reconstructed density profile of a nitrogen gas-jet at room temperature with a primary pressure of $p_0 = 12.5$ bar expanding into a vacuum of $p = 1.02$ mbar. 100 pixels correspond to 1.18 mm.

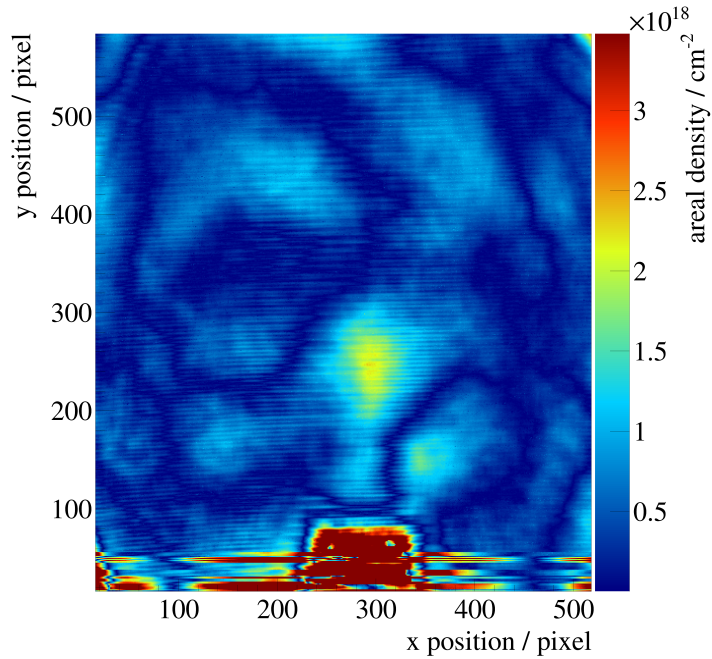


Figure A.9 – Reconstructed density profile of a nitrogen gas-jet at room temperature with a primary pressure of $p_0 = 13$ bar expanding into a vacuum of $p = 1.06$ mbar. 100 pixels correspond to 1.18 mm.

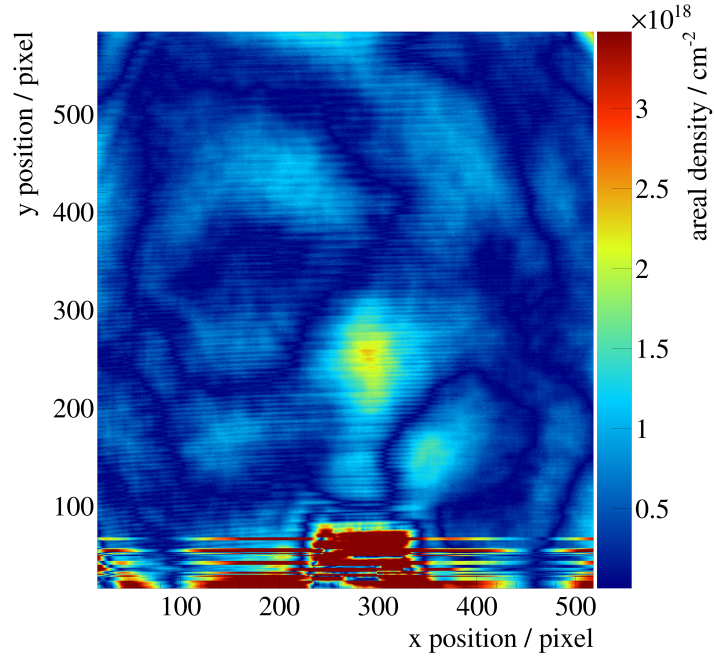


Figure A.10 – Reconstructed density profile of a nitrogen gas-jet at room temperature with a primary pressure of $p_0 = 13.5$ bar expanding into a vacuum of $p = 1.10$ mbar. 100 pixels correspond to 1.18 mm.

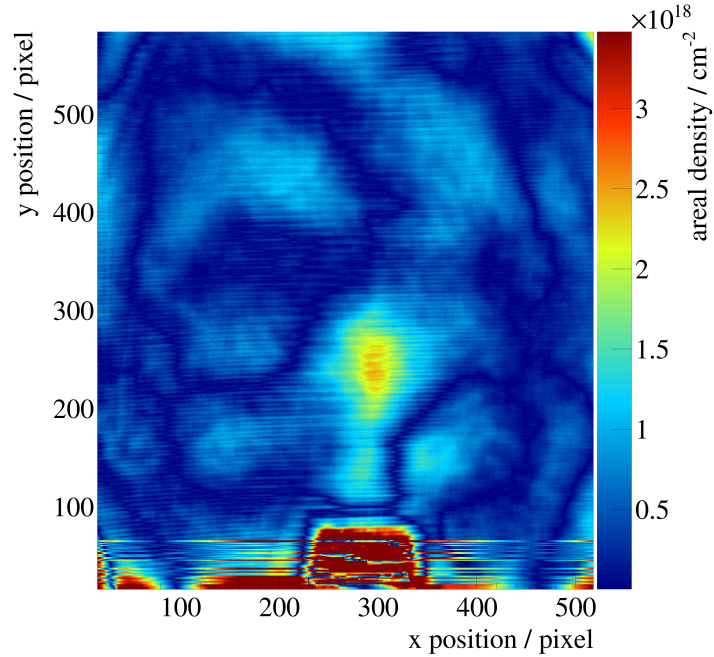


Figure A.11 – Reconstructed density profile of a nitrogen gas-jet at room temperature with a primary pressure of $p_0 = 14$ bar expanding into a vacuum of $p = 1.15$ mbar. 100 pixels correspond to 1.18 mm.

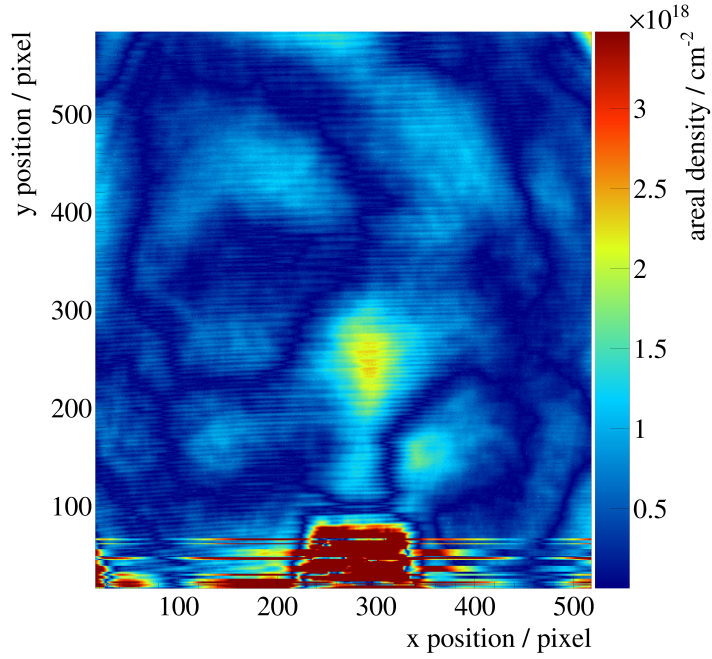


Figure A.12 – Reconstructed density profile of a nitrogen gas-jet at room temperature with a primary pressure of $p_0 = 14.5$ bar expanding into a vacuum of $p = 1.19$ mbar. 100 pixels correspond to 1.18 mm.

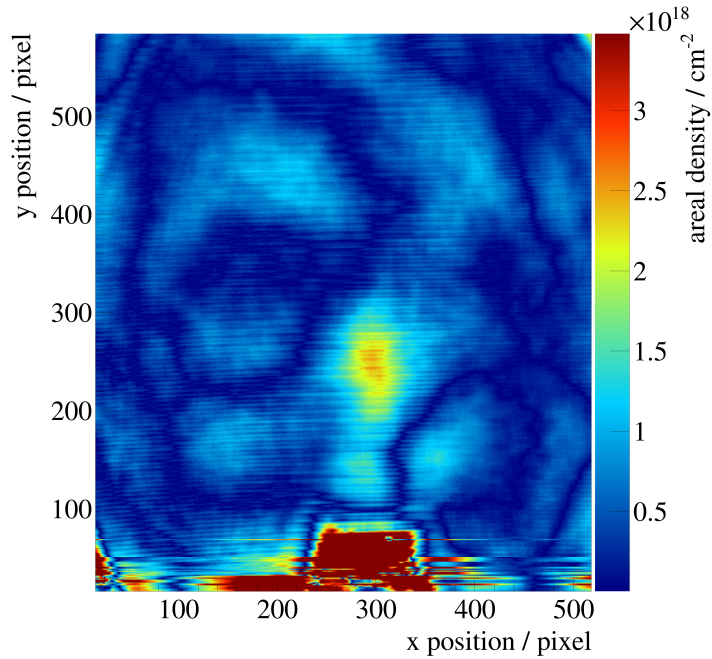


Figure A.13 – Reconstructed density profile of a nitrogen gas-jet at room temperature with a primary pressure of $p_0 = 15$ bar expanding into a vacuum of $p = 1.24$ mbar. 100 pixels correspond to 1.18 mm.

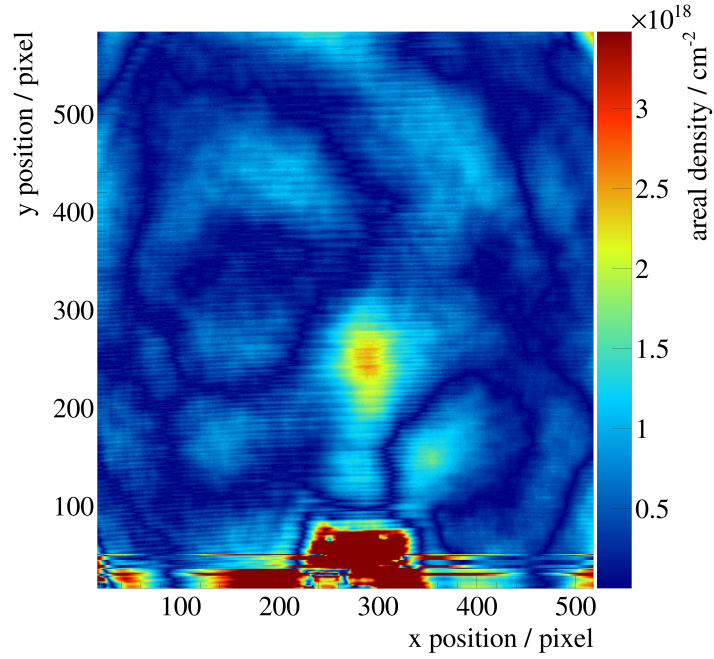


Figure A.14 – Reconstructed density profile of a nitrogen gas-jet at room temperature with a primary pressure of $p_0 = 15.5$ bar expanding into a vacuum of $p = 1.28$ mbar. 100 pixels correspond to 1.18 mm.

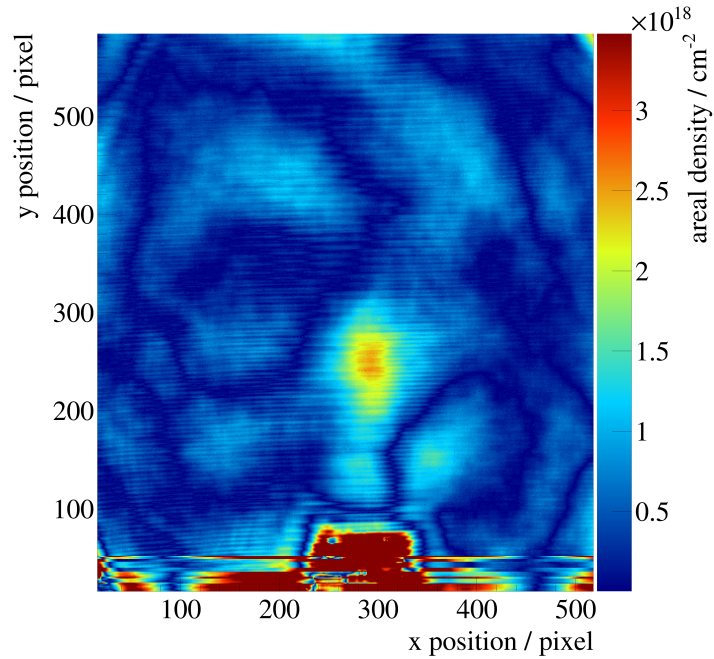


Figure A.15 – Reconstructed density profile of a nitrogen gas-jet at room temperature with a primary pressure of $p_0 = 16$ bar expanding into a vacuum of $p = 1.33$ mbar. 100 pixels correspond to 1.18 mm.

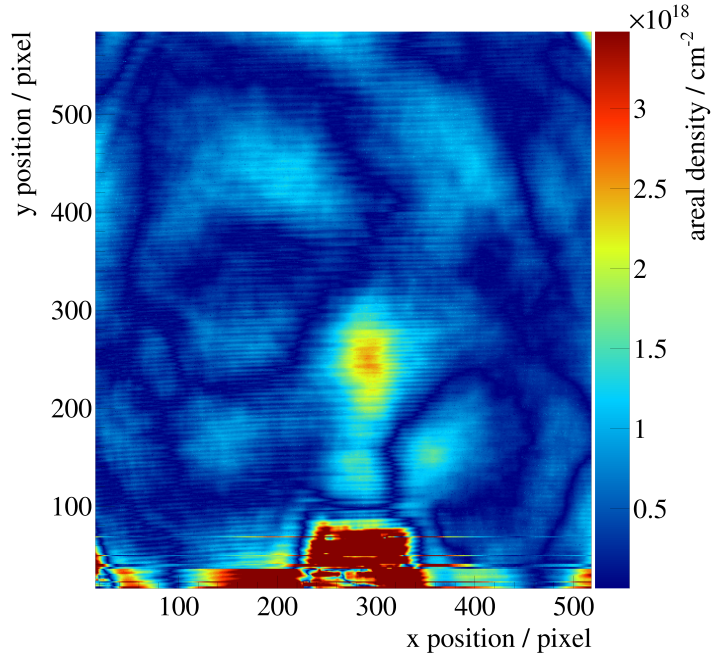


Figure A.16 – Reconstructed density profile of a nitrogen gas-jet at room temperature with a primary pressure of $p_0 = 16.5$ bar expanding into a vacuum of $p = 1.37$ mbar. 100 pixels correspond to 1.18 mm.

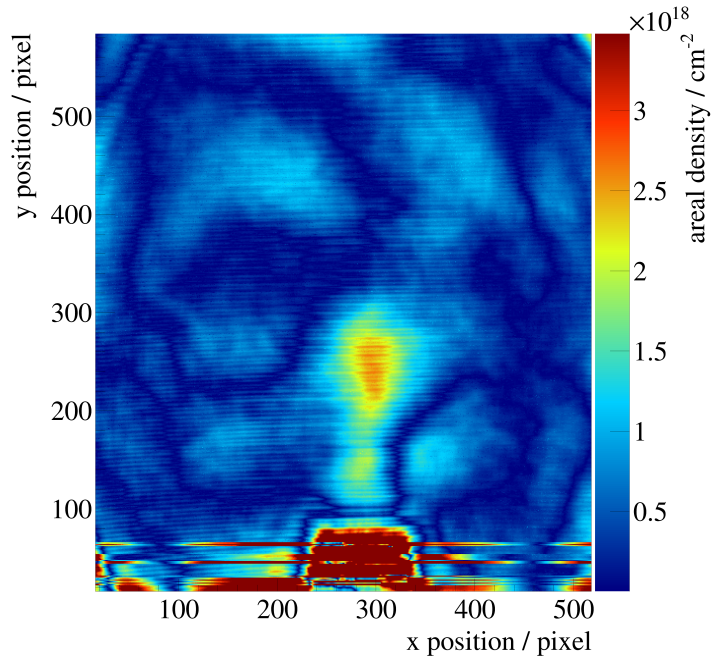


Figure A.17 – Reconstructed density profile of a nitrogen gas-jet at room temperature with a primary pressure of $p_0 = 17$ bar expanding into a vacuum of $p = 1.42$ mbar. 100 pixels correspond to 1.18 mm.

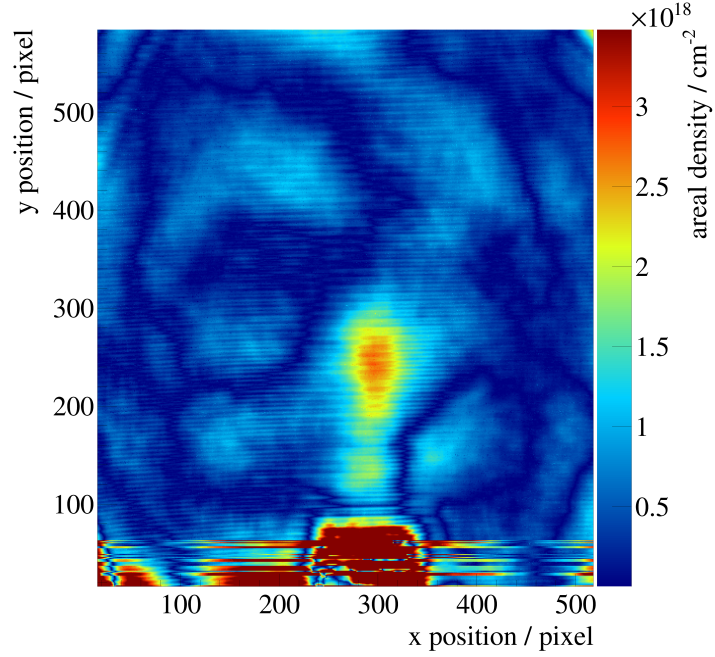


Figure A.18 – Reconstructed density profile of a nitrogen gas-jet at room temperature with a primary pressure of $p_0 = 17.5$ bar expanding into a vacuum of $p = 1.45$ mbar. 100 pixels correspond to 1.18 mm.

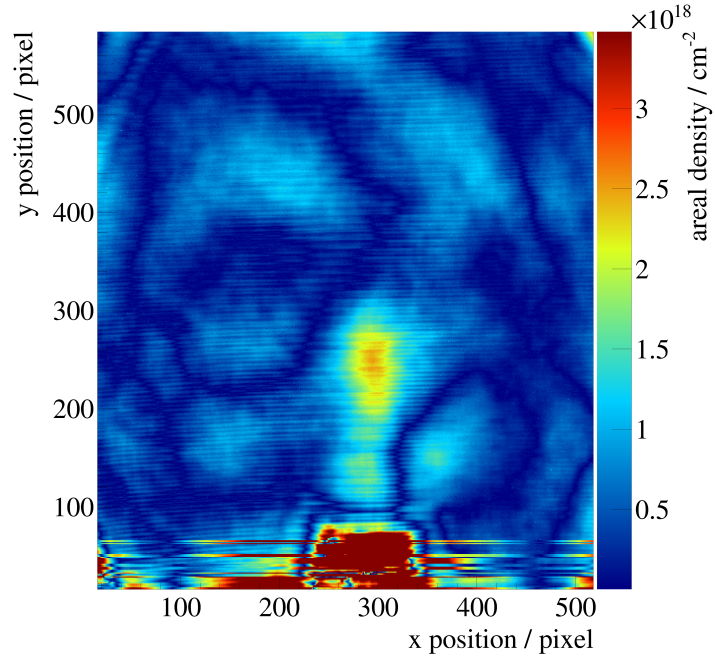


Figure A.19 – Reconstructed density profile of a nitrogen gas-jet at room temperature with a primary pressure of $p_0 = 18$ bar expanding into a vacuum of $p = 1.50$ mbar. 100 pixels correspond to 1.18 mm.

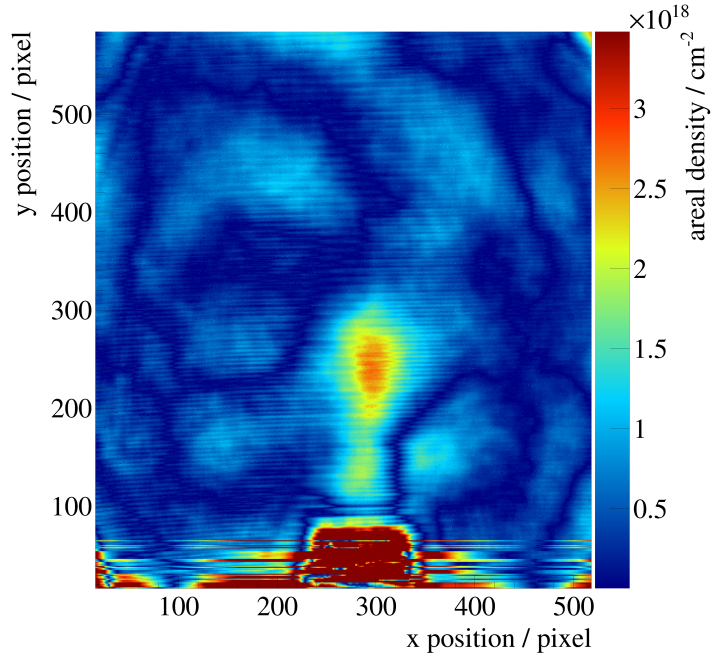


Figure A.20 – Reconstructed density profile of a nitrogen gas-jet at room temperature with a primary pressure of $p_0 = 18.5$ bar expanding into a vacuum of $p = 1.53$ mbar. 100 pixels correspond to 1.18 mm.

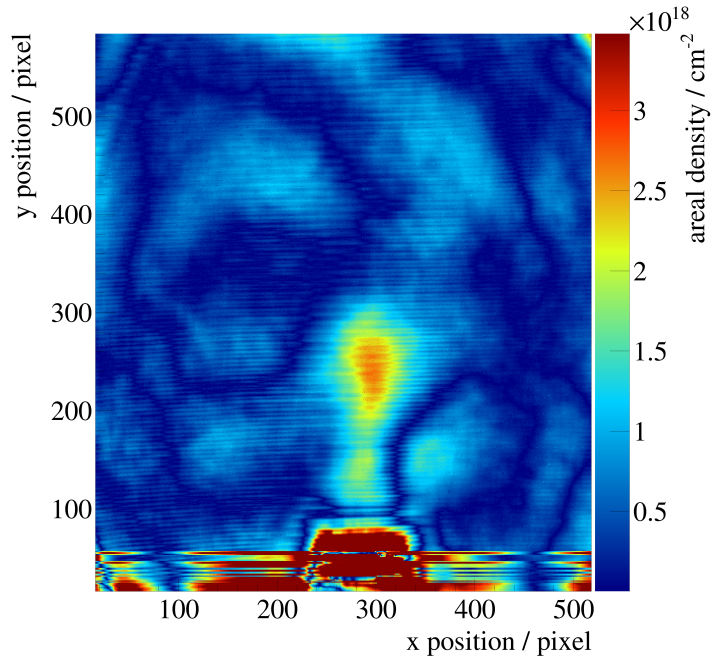


Figure A.21 – Reconstructed density profile of a nitrogen gas-jet at room temperature with a primary pressure of $p_0 = 19$ bar expanding into a vacuum of $p = 1.59$ mbar. 100 pixels correspond to 1.18 mm.

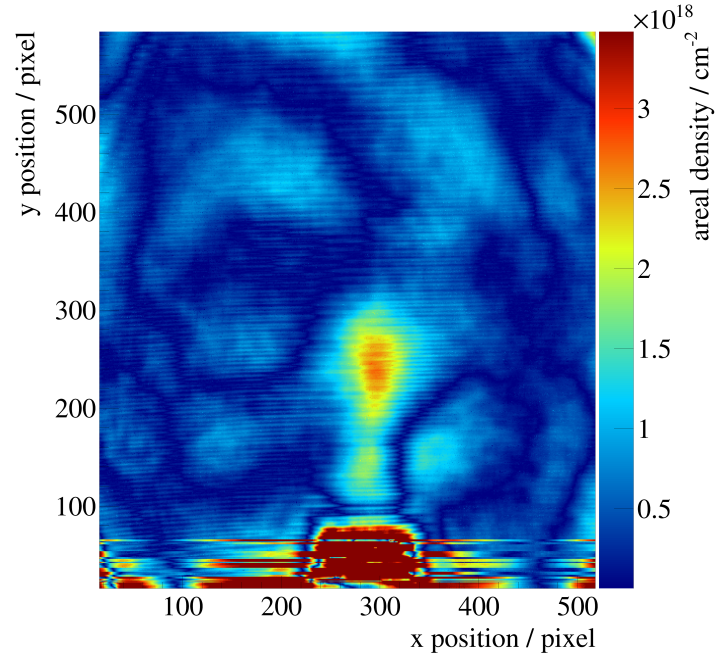


Figure A.22 – Reconstructed density profile of a nitrogen gas-jet at room temperature with a primary pressure of $p_0 = 19.5$ bar expanding into a vacuum of $p = 1.63$ mbar. 100 pixels correspond to 1.18 mm.

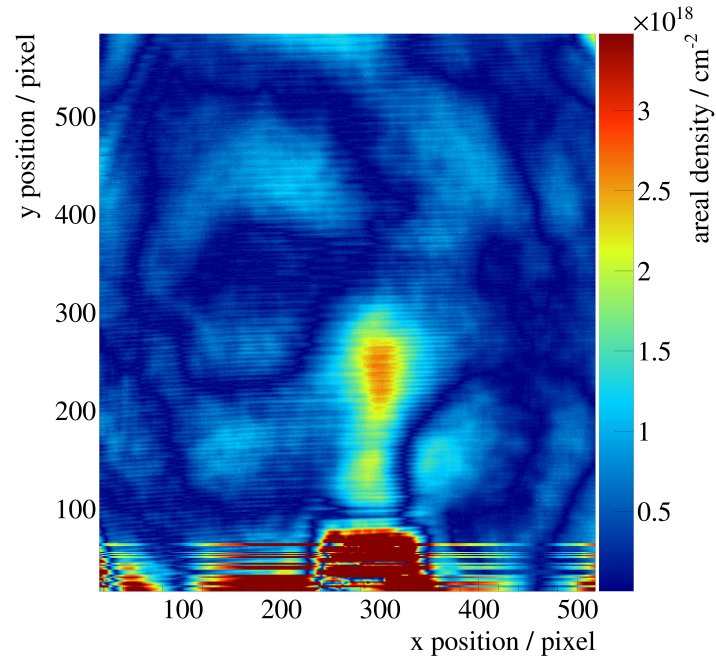


Figure A.23 – Reconstructed density profile of a nitrogen gas-jet at room temperature with a primary pressure of $p_0 = 20$ bar expanding into a vacuum of $p = 1.66$ mbar. 100 pixels correspond to 1.18 mm.

Table A.1 – Listing of the different pressures in the interaction chamber p_{iac} and the maximal reconstructed areal densities $\rho_{\text{A, max}}$ for different pressures in front of the nozzle p_0 . The uncertainties for the reconstructed areal densities are at least 5% – 10% (s. 6.2)

p_0/bar	$p_{\text{iac}}/\text{mbar}$	$\rho_{\text{A, max}}/\text{cm}^{-2}$
0.3(1)	0.01(1)	$1.6 \cdot 10^{18}$
9.5(1)	0.70(1)	$2.1 \cdot 10^{18}$
10.0(1)	0.81(1)	$2.0 \cdot 10^{18}$
10.5(1)	0.84(1)	$2.2 \cdot 10^{18}$
11.0(1)	0.89(1)	$2.1 \cdot 10^{18}$
11.5(1)	0.94(1)	$2.5 \cdot 10^{18}$
12.0(1)	0.98(1)	$2.3 \cdot 10^{18}$
12.5(1)	1.02(1)	$2.5 \cdot 10^{18}$
13.0(1)	1.06(1)	$2.3 \cdot 10^{18}$
13.5(1)	1.10(1)	$2.4 \cdot 10^{18}$
14.0(1)	1.15(1)	$2.5 \cdot 10^{18}$
14.5(1)	1.19(1)	$2.4 \cdot 10^{18}$
15.0(1)	1.24(1)	$2.6 \cdot 10^{18}$
15.5(1)	1.28(1)	$2.6 \cdot 10^{18}$
16.0(1)	1.33(1)	$2.6 \cdot 10^{18}$
16.5(1)	1.37(1)	$2.7 \cdot 10^{18}$
17.0(1)	1.42(1)	$2.7 \cdot 10^{18}$
17.5(1)	1.45(1)	$2.9 \cdot 10^{18}$
18.0(1)	1.50(1)	$2.6 \cdot 10^{18}$
18.5(1)	1.53(1)	$2.9 \cdot 10^{18}$
19.0(1)	1.59(1)	$2.7 \cdot 10^{18}$
19.5(1)	1.63(1)	$2.8 \cdot 10^{18}$
20.0(1)	1.66(1)	$2.7 \cdot 10^{18}$

Bibliography

- [A⁺94] H.G. Andresen et al. The mami-beam of polarized electrons. In *Proceedings, EPAC 1994, London p.1483*, 1994.
- [Aul14] Stephan Aulenbacher. *Design and Simulation of the Internal Gas-Target for MAGIX*. Diploma thesis, Johannes Gutenberg-Universität Mainz, 2014.
- [B⁺09] Matthew Baumgart et al. Non-abelian dark sectors and their collider signatures. *Journal of High Energy Physics*, (number 04):p.14, 2009.
- [B⁺13] S.J. Brodsky et al. Physics opportunities of a fixed-target experiment using lh beams. *Physics Reports*, volume 522(number 4):p.239–255, 2013.
- [B⁺15] Niklaus Berger et al. Measuring the weak mixing angle with the p2 experiment at mesa. *arXiv:1511.03934*, 2015.
- [Bal17] Robin Balske. Bachelor’s thesis, Westfälische Wilhelms-Universität Münster, 2017. In progress.
- [Ber02] Christoph Berger. *Elementarteilchenphysik*. Springer-Verlag, 2002. ISBN: 978-3-642-41753-5.
- [BGS16] R. Bucoveanu, M. Gorchtein, and H. Spiesberger. Precision measurement of $\sin^2(\theta_w)$ at mesa. *arXiv:1606.09268*, 2016.
- [Car15] Carl E. Carlson. The proton radius puzzle. *Progress in Particle and Nuclear Physics*, volume 82:p.59–77, 2015.
- [Che11] Kirby Cheng. <http://kirbycheng.blogspot.de/2011/07/activity-7-properties-of-2d-fourier.html>, 2011. Access: 17.10.2016.
- [Dem09] W. Demtröder. *Experimentalphysik 2, Elektrizität und Optik*. Springer-Verlag, 2009. ISBN: 978-3-540-68210-3.

- [EE15] Hans Joachim Eichler and Jürgen Eichler. *Laser: Bauformen, Strahlführung, Anwendungen*. Springer-Verlag, 2015. ISBN: 978-3-642-10462-6.
- [Eks95] C. Ekström. Internal targets - a review. *Nuclear Instruments and Methods in Physics Research A*, volume 362:p.1–15, feb 1995.
- [F⁺11] Hannes Fulge et al. Improved abel inversion method for analysis of spectral and photo-optical data of magnetic influenced plasma flows. In *42nd AIAA Plasmadynamics and Lasers Conference, June 27.-30., 2011*.
- [FB08] Thomas Frey and Martin Bossert. *Signal-und Systemtheorie*, volume 2. Springer-Verlag, 2008. ISBN: 978-3-8348-9292-8.
- [Fri15] Friederich, Simon and Aulenbacher, Kurt. Test electron source for increased brightness emission by near band gap photoemission. In *Proceedings, 6th International Particle Accelerator Conference (IPAC 2015): Richmond, Virginia, USA, May 3-8, 2015*, page 44, 2015.
- [Gel74] E. Gelfort. Das separationsvermögen des wien-filters. *International Journal of Mass Spectrometry and Ion Physics*, volume 14(number 4):p.349–361, August 1974.
- [Gri17] Silke Grieser. PhD thesis, Westfälische Wilhelms-Universität Münster, 2017. In progress.
- [H⁺15] R. Heine et al. Further investigations on the mesa injector. In *IPAC'15, Richmond, USA, p.45*, 2015.
- [Har16] Catharina Hargens. *Aufbau und Inbetriebnahme eines Gas-Jet Targets für MAGIX @ MESA sowie die Justage eines Cluster-Jet Targets für Laserstreuexperimente*. Bachelor's thesis, Westfälische Wilhelms-Universität Münster, 2016.
- [HM03] Werner Herr and Bruno Muratori. Concept of luminosity. In *proceedings of CERN Accelerator School*, volume 361, 2003.
- [JS13] Gerhart Jander and Hans Spandau. *Kurzes Lehrbuch der anorganischen und allgemeinen Chemie*. Springer-Verlag, 2013. ISBN: 978-3-540-16749-5.
- [KS08] Fritz Kurt Kneubühl and Markus Werner Sigrist. *Laser*. Springer-Verlag, 2008. ISBN: 978-3-8351-0145-6.

- [Laz] Josef Lazar. Metrology of time and length - a question of radio and optical frequencies. Presentation.
- [Ley07] Leybold. *Grundlagen der Vakuumtechnik*. Kat.-Nr. 199 89, 2007.
- [LHH07] Xian-Fang Li, Li Huang, and Yong Huang. A new abel inversion by means of the integrals of an input function with noise. *Journal of Physics A: Mathematical and Theoretical*, volume 40(number 2):p.347, 2007.
- [M⁺00] Victor Malka et al. Characterization of neutral density profile in a wide range of pressure of cylindrical pulsed gas jets. *Review of Scientific Instruments*, volume 71(number 6):p.2329–2333, 2000.
- [M⁺11] D. Munday et al. Flow structure and acoustics of supersonic jets from conical convergent-divergent nozzles. *Physics of Fluids (1994-present)*, volume 23(number 11):p.116102, 2011.
- [MAG16] <http://wwwa1.kph.uni-mainz.de/magix/index.html>, 2016. Access: 22.09.2016.
- [Mbu13] Jean-Baptiste Mulumba Mbuyamba. *Calculation and design of supersonic nozzles for cold gas dynamic spraying using MATLAB and ANSYS Fluent*. PhD thesis, University of the Witwatersrand, Johannesburg, 2013.
- [Mes09] Dieter Meschede. *Optik, Licht und Laser*. Springer-Verlag, 2009. ISBN: 978-3-8348-9288-1.
- [MES16] <http://www.mesa.uni-mainz.de/index.php>, 2016. Access: 22.09.2016.
- [MLR] E.D. Marquardt, J.P. Le, and Ray Radebaugh. *Cryogenic Material Properties Database*.
- [MTN12] Peter J Mohr, Barry N Taylor, and David B Newell. Codata recommended values of the fundamental physical constants: 2010a). *Journal of Physical and Chemical Reference Data*, volume 41(number 4):p.043109, 2012.
- [Mül14] Julian Müller. *Entwurf eines Spektrometers für Niederenergieexperimente an MESA*. Diploma thesis, Johannes Gutenberg-Universität Mainz, 2014.
- [Np116] <https://www.newport.com/n/spatial-filters>, 2016. Access: 25.10.2016.

- [R⁺97] H. Reich et al. The esr internal target. *Nuclear Physics A*, volume 626(number 1):p.417–425, 1997.
- [Rau16] Julian Rausch. *Entwicklung einer interferometrischen Methode zur Messung des Gas-Jet-Dichteprofiles am MAGIX-Experiment*. Bachelor’s thesis, Johannes Gutenberg-Universität Mainz, 2016.
- [RKH10] K.R. Rao, D.N. Kim, and J.J. Hwang. *Two-Dimensional Discrete Fourier Transform*. Springer-Verlag, 2010. ISBN: 978-1-4020-6628-3.
- [RS92] J. Rossbach and Peter Schmueser. Basic course on accelerator optics. In *Conf. Proc.*, volume 9209071, pages 17–88, 1992.
- [S⁺15] Timo Stengler et al. Modified elbe type cryomodules for the mainz energy-recovering superconducting accelerator mesa. In *17th International Conference on RF Superconductivity (SRF2015), Whistler, BC, Canada, Sept. 13-18, 2015*, pages 1413–1416. JACOW, Geneva, Switzerland, 2015.
- [Sau16] Fabio Sauli. The gas electron multiplier (gem): Operating principles and applications. *Nuclear Instruments and Methods in Physics Research Section A: Accelerators, Spectrometers, Detectors and Associated Equipment*, volume 805:p.2–24, 2016. Special Issue in memory of Glenn F. Knoll.
- [Sch13] Franz Schwabl. *Quantenmechanik*. Springer-Verlag, 2013.
- [Sim14] Daniel Simon. *Strahlführungsdesign für MESA*. Diploma thesis, Johannes Gutenberg-Universität Mainz, 2014.
- [SV12] Karl Schmid and László Veisz. Supersonic gas jets for laser-plasma experiments. *Review of Scientific Instruments*, volume 83(number 5):p.053304, 2012.
- [Täs12] Alexander Täschner. *Entwicklung und Untersuchung von Cluster-Jet-Targets höchster Dichte*. PhD thesis, Westfälische Wilhelms-Universität Münster, 2012.
- [Tho99] https://www.thorlabs.com/newgrouppage9.cfm?objectgroup_id=1400, 1999. Access: 18.10.2016.
- [Wei94] Mario Weiss. Introduction to rf linear accelerators. *CERN European Organization for Nuclear Research-Reports-CERN*, pages 913–913, 1994.

- [Wes16] Christina Westphälinger. *Mach-Zehnder-Interferometer zur Dichtebestimmung eines Gas-Jet Targets*. Bachelor's thesis, Westfälische Wilhelms-Universität Münster, 2016.
- [Wik08] https://en.wikipedia.org/wiki/De_Laval_nozzle, 2008. Access: 23.09.2016.
- [Wil96] Klaus Wille. *Physik der Teilchenbeschleuniger und Synchrotronstrahlungsquellen*. Springer Fachmedien Wiesbaden GmbH, 1996. ISBN: 978-3-540-52359-8.
- [Z⁺11] Magdalena Zych et al. Quantum interferometric visibility as a witness of general relativistic proper time. *Nature communications*, volume 2(number 505), 2011.

Acknowledgements

Finally i would like to thank everyone who contributed realising this work or supported me doing it.

First of all i would like to thank my examiner Prof. Dr. A. Khoukaz who suggested the subject of my work, showed a constant interest in my progress and always had council and an open ear for me.

Sincere thanks are given to my supervisor Silke Grieser for her working instructions, support, feedback, all the proofreading and the wonderful cooperation.

I would like to thank Dr. C. Klein-Bösing for being my second examiner.

I am obliged to Daniel Bonaventura for helping me building the experimental setup and all its components and for being my helping hand for everything that went wrong. I would also like to thank G. Bourichter and the mechanical workshop just like R. Berendes and the electronics workshop for their fast work and repairs.

Special thanks goes to Stephan Fortmeier for proofreading and spell checking my whole work, no one could read it without all the commas you added!

I also like to thank Christina Westphälinger for all the groundwork on our Mach-Zehnder interferometer and Dr. J. Imbrock from the department of applied physics for answering all my questions about interferometers and for his huge support concerning spatial filters.

Many thanks goes to Benjamin Hetz, Nils Hüsken and Kay Demmich for all the programming support.

I would like to thank the people of my working group Ann-Katrin, Florian, Kay, Silke, Benny, Cathi, Robin, Christina, Marcel, Daniel, Christopher and Nils for the nice working atmosphere, the shared lunch time and all the activities not concerning our work.

I must not forget to thank my coffee break companions Kay, Daniel and Micky. I really enjoyed the time with you.

Last but not least i am obliged to my friends, my family and my girlfriend Laura for their constant support, their trust in my skills and their offered distraction when i needed it.

Declaration of Academic Integrity

I hereby confirm that this thesis on *Investigations on gas jet beam profiles with a Mach-Zehnder interferometer* is solely my own work and that I have used no sources or aids other than the ones stated. All passages in my thesis for which other sources, including electronic media, have been used, be it direct quotes or content references, have been acknowledged as such and the sources cited.

(date and signature of student)

I agree to have my thesis checked in order to rule out potential similarities with other works and to have my thesis stored in a database for this purpose.

(date and signature of student)